ADVANCED FUNCTIONAL MATERIALS

www.afm-journal.de

A Review on Principles and Applications of Scanning Thermal Microscopy (SThM)

Yun Zhang, Wenkai Zhu, Fei Hui, Mario Lanza, Theodorian Borca-Tasciuc, and Miguel Muñoz Rojo**

As the size of materials, particles, and devices shrinks to nanometer, atomic, or even quantum scale, it is more challenging to characterize their thermal properties reliably. Scanning thermal microscopy (SThM) is an emerging method to obtain local thermal information by controlling and monitoring probe–sample thermal exchange processes. In this review, key experimental and theoretical components of the SThM system are discussed, including thermal probes and experimental methods, heat transfer mechanisms, calibration strategies, thermal exchange resistance, and effective heat transfer coefficients. Additionally, recent applications of SThM to novel materials and devices are reviewed, with emphasis on thermoelectric, biological, phase change, and 2D materials.

1. Introduction

At the beginning of 21st century, researchers started to dive deeper into the miniaturized world. In the fields of chemical synthesis, biomedical research, mechanical failure management, and electronics, the capability to explore, measure, modify, and ultimately manufacture in the nanoworld is increasingly demanding. Device feature sizes were reduced to very small length scales, only a few-to-tens of nanometers, and shorter time domains were needed to observe fast transport and energy conversion phenomena.[1] Scanning thermal microscopy (SThM) was developed based on scanning probe microscopy (SPM)[2] and is one of the experimental techniques enabling the understanding of nanoscale thermal phenomena. Direct observation of physical thermal transport phenomena requires SThM with a high temporal and spatial resolution (milli- to microsecond thermal time constant and nanoscale lateral resolution).[3] SThM in a broad sense is based on a thermally active or thermally sensitive probe placed on an AFM head where either laser-mirror-photodetector combination on cantilever or a piezoelectric cantilever is used to detect nanoscale deflections, thus sensing the tip–sample interaction force.[4] The SThM probe, a nanoscale thermocouple or resistor in most cases can operate in what is called the *active mode*, also referred as conductivity contrast mode (CCM),[5] or in the *passive mode* called temperature contrast mode (TCM), also known as sensing mode. In the *active mode* the probe acts as a local heater. It is heated up by an external source such as laser heating or an internal source through Joule heating and can be further subdivided into constant current mode and constant temperature mode. The *passive mode* refers to the case when the probe acts like a temperature sensor with minimal heating power dissipated.[6] SThM measurements can be performed both in contact and noncontact mode. In contact mode, a mechanical contact is established between the probe tip and the sample surface, while in noncontact mode the probe usually operates a few tens to hundreds of nanometers above sample surface.[7] One special case is when the SThM probe is used to measure materials' phase-transition temperature, mostly for polymers. In this scenario, the probe is in the active plus contact mode and monitors vertical displacement and temperature of the probe simultaneously.[8] After implementing careful calibration procedures, *passive mode* SThM (Passive-SThM) senses sample surface temperature distribution[9] and *active mode* SThM (Active-SThM) can be used to measure samples' thermal properties, such as thermal conductivity, *k,* and Seebeck Coefficient, *S*, as well as to perform surface lithography using special high temperature probes.[1b,9b,10] Manufacturing with scanning probes is not included in this review, which focuses on thermal measurements with SThM.

Y. Zhang, W. Zhu, Prof. T. Borca-Tasciuc
Mechanical, Aerospace and Nuclear Engineering Department
Rensselaer Polytechnic Institute
110 Eighth Street, Troy, NY 12180, USA
E-mail: borcat@rpi.edu

F. Hui
Department of Materials Science and Engineering
Technion-Israel Institute of Technology
Haifa 32000, Israel

F. Hui
Department of Materials Science and Engineering
Guangdong Technion-Israel Institute of Technology
241 Daxue Road, Jinping District, Shantou 515063, China

Prof. M. Lanza
Institute of Functional Nano and Soft Materials
Collaborative Innovation Center of Suzhou Nanoscience and Technology
Soochow University
199 Ren-Ai Road, Suzhou 215123, China

Dr. M. Muñoz Rojo
Department of Thermal and Fluid Engineering
University of Twente
Enschede 7500 AE, The Netherlands
E-mail: m.munozrojo@utwente.nl

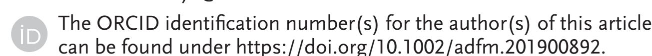
The ORCID identification number(s) for the author(s) of this article can be found under https://doi.org/10.1002/adfm.201900892.

© 2019 The Authors. Published by WILEY-VCH Verlag GmbH & Co. KGaA, Weinheim. This is an open access article under the terms of the Creative Commons Attribution License, which permits use, distribution and reproduction in any medium, provided the original work is properly cited.

DOI: 10.1002/adfm.201900892

© 2019 The Authors. Published by WILEY-VCH Verlag GmbH & Co. KGaA, Weinheim

However, SThM still poses key challenges. One challenge is modeling the heat transfer between SThM probes and samples, especially in the transition to fully ballistic regimes for the heat transport across the tip–sample contact region. In these regimes, the diffusion heat transport equations cannot be used anymore.[11] Second modeling challenge is considering the near-field radiation mechanism for SThM, which may be critical for measurements performed in vacuum environment.[12] The third is a experimental challenge, quantitative thermal conductivity characterization by commercial systems is not widely available[13] due to the difference in temperatures between the probe and the sample[10c] coupled with insufficient implementation of effective calibration techniques for tip–sample thermal exchange parameters. Several calibration strategies developed by researchers are discussed here. Fourth, while new nanoscale thermal probes proved to improve the time resolution achieving less than 1 ms time response,[1c,2] multifunctional probes still need to be developed to enable simultaneous characterization of thermal and nanoscale,[14] magnetic,[15] chemical,[16] and mechanical properties,[15,17] as shown by other SPM applications with multifunctional probes.[10c] Finally, despite its high temperature sensitivity, SThM is vulnerable to topographical artifacts, wear and tear, which leads to inaccurate results when a constant probe–sample thermal exchange resistance is typically assumed by heat transfer models.[18] The thermal conductivity imaged by SThM may not accurately reflect the sample thermal conductivity due to the artifacts originated from the tip–sample contact which are typically induced by sample surface roughness.[1c] The SThM with carbon nanotubes (CNT) as thermal tips[1e] provides superior sensitivity and enables reducing the topography artifacts. However, it has reduced performance when the tip wears, so artifacts-related problems may still need to be considered.[19] Thus, development of improved probe designs and batch fabrication technologies are critical to resolve topographical artifacts related problems and provide more reliable SThM characterization.

Compared to other SPM and traditional microscopies, SThM currently has several limitations. SThM techniques are not well adapted to image biological cells due to its slow scanning speed and are seldom used for operation under liquid environments,[20] unlike plasmonic thermal microscopy.[21] Additionally, compared to scanning joule expansion microscopy (SJEM) and polymer imprint thermal mapping, SThM signals were disturbed when measuring nanoscale temperature profiles around plasmonic antenna in heat-assisted magnetic reading.[22] Optical thermometry such as fluorescence thermal mapping and IR spectroscopy has the ability to penetrate different media with minimal perturbation and can be implemented in a wide range of applications.[23] However, SThM requires additional effort to develop matching qualities.[22]

This review presents some novelties in comparison to previous ones.[10c,18a,24] On one hand it discusses some of the most recently published papers, between 2012 and 2019. Second, it focuses on an extended analysis of the fundamentals of the SThM, including calibration methods for the heat transfer parameters between the sample and the probe. Third, this review discusses the applicability of SThM to measure a variety of materials and devices, making SThM an emerging technique in areas such as electronics or biology.

Yun Zhang received her M.S. degree in thermal engineering from Xi'an Jiaotong University. She then pursued for the Ph.D. degree of Mechanical Engineering in Rensselaer Polytechnic Institute. Her research focuses on analytical modeling, numerical simulation, and experiments in the field of scanning thermal probe metrology.

Theodorian Borca-Tasciuc has a B.S. in physics from Bucharest University and a PhD in mechanical engineering from University of California Los Angeles. He is a professor at Rensselaer Polytechnic Institute where he teaches in thermal and fluids fields and directs research in energy conversion materials, devices and systems.

Miguel Muñoz Rojo received his Ph.D. degree in condensed matter physics and nanotechnology and his M.S./B.S. degree in physics from the Autonomous University of Madrid. Afterward, he became a postdoctoral researcher at Stanford University. He is currently an Assistant Professor in the department of Thermal and Fluid engineering at the University of Twente. His current research focus is the transport properties of novel 3D, 2D, and 1D materials and their applications in thermal and electrical devices.

This SThM review is divided in specialized sections discussing fundamentals and the most recent updates. Section 2 briefly discusses the history and general principles of SThM and then covers details of key experimental components of SThM, including probes, electric bridge circuits, and system setups. Section 3 discusses four major heat transfer mechanisms that occur in ambient SThM, conduction through air, through water meniscus, and through solid–solid contact, and radiation heat transfer, with emphasis on air and solid–solid conduction.[25] Diffusive and ballistic air conduction regimes are distinguished depending on tip–sample clearance with respect to the mean free path (MFP),[3b] which are important for establishing accurate

© 2019 The Authors. Published by WILEY-VCH Verlag GmbH & Co. KGaA, Weinheim

models for SThM. The singular and uniform contact assumption in solid–solid conduction was challenged, and an alternative decomposition to study solid–solid conduction was proposed.[26] Due to variety of SThM setups, one or more heat transfer paths may be closed or neglected. There is no established agreement on the dominant heat transfer mechanisms and several representative works will be discussed in this section. Section 4 reviews SThM calibration, which includes absolute calibration against reference materials and determination of sample thermal conductivity.[2] This section is divided into five parts, discussing the sample calibration, probe parameter calibration, and thermal exchange parameter calibration. Section 5 focuses on current major areas of applications, including measuring thermal properties of novel materials and devices and observing novel nanoscale heat transport phenomena. 2D materials are on top of the investigative interest list due to their unique thermal properties,[27] with key applications in microscale and nanoscale electronics. In recent studies, SThM has been used to measure different types of electronic devices, such as phase change memory (PCM) or resistive random-access memory (RRAM) that gathered attention as strong candidates for nonvolatile memory devices and for possibility of further memory miniaturization.[28] Nanoscale heat transfer phenomena due to electrocaloric effect (EC) and thermoelectric effect are also revealed by improvement of the characterization ability of SThM with nanoscale resolution.

2. Instrumentation of SThM

2.1. Brief History and Principle Operation of SThM

Since the late 1980s, Williams and Wickramasinghe[29] studied the scanning thermal profiler (SThP), which was at the origin of SThM. The working mechanism of SThP is almost the same as scanning tunneling microscopy (STM). However, a key difference is that a constant heat flux is used to maintain tip–sample distance (in SThP) instead of tunneling current (in STM). In this system, a nano-thermocouple was used as the probe and the temperature difference as the feedback mechanism for tip–sample distance. The spatial resolution achieved was a few hundred nanometers. The authors investigated both material properties and surface temperature.[29] In 1990s, SThM systems with simultaneous collection of thermal images and topography were established. In 1993, Majumdar, Carrejo and Lai[30] constructed a K-type thermocouple based SThM used for simultaneous mapping of surface temperature and surface topography. In the next few decades, more development of SThM techniques focused on new thermal probe tips. In 1994, Dinwiddie, Pylkki, and West[31] developed the metallic resistive Wollaston probe known for its wide applicability and high endurance. The SThM working system using thermistor probes is illustrated in **Figure 1**. Microthermal analysis (μTA)[23a] and nanothermal analysis (nano-TA) were developed with new Palladium (Pd) on SiN_x probes and doped silicon (DS) probes, being able to perform nanoscale thermal scanning at fast rate.[32]

Common thermal probe sensing mechanisms are: Seebeck thermovoltage,[33] variation in electrical resistance,[7a,32,34] fluorescence,[35] or thermal expansion.[36] **Table 1** shows a

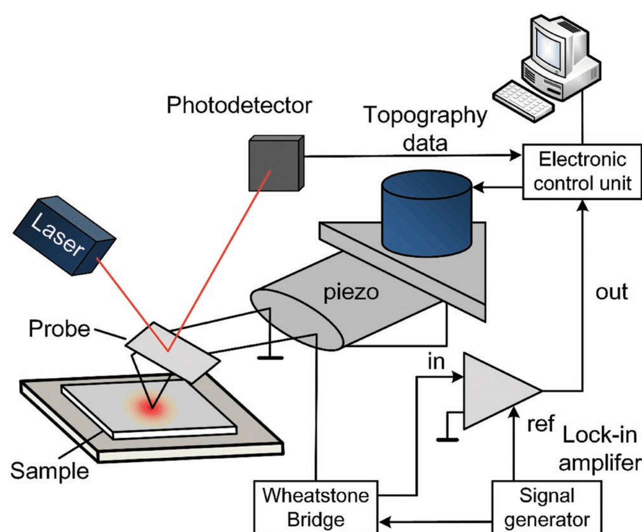

Figure 1. Schematic diagram of SThM setup. The photodetector and laser are used to detect the probe position and contact force through the cantilever deflection measured by the laser reflection. Wheatstone bridge details are discussed in Section 2.5.1. Adapted with permission.[38b] Copyright 2013, Elsevier.

comparison of SThM probe types based on their sensing mechanism, including materials used for the probes, spatial and temperature resolution, thermal time constant, and other operating parameters.

The thermal probe is the heart of an SThM system that determines its capability, range of operation and quality of measurement. The most critical parameters of an SThM probe, whether it is a thermoelectric or resistive based probe, are the tip radius and probe material. Tip radius limits the spatial resolution[2] and also constricts the amount of heat transferred between tip and sample.[1b] The materials from which the probe tip is made directly affect the performance of SThM measurement, as they control the thermal transduction mechanism. SThM probes could be made compatible with systems that enable optical properties measurements when combined with IR. With different system setups, SThM probes demonstrated enhancing measurement capability.[9a,20b,42] These types of probes plus few more will be elaborated in the following sections.

2.2. Thermoresistive SThM Probes

Thermoresistive probes use a resistor as a thermal sensor, including metallic thin film, metallic bent wire, or highly doped semiconductor resistor probe. Platinum (Pt), platinum alloy (Pt90/Rh10), and palladium (Pd) are the materials typically used for metal-based thermoresistive or thermistor probes due to its high temperature coefficient of resistivity (TCR) and high resistivity. Semiconductor probes are usually made of silicon.[18b,38e]

2.2.1. Principle of Thermoresistive Probe

Passive-SThM: To measure the probe electrical resistance, a current small enough to neglect the probe temperature rise due

© 2019 The Authors. Published by WILEY-VCH Verlag GmbH & Co. KGaA, Weinheim

Table 1. Thermal probes comparison. The thermal time constant, temperature resolution, and thermal sensitivity are defined in ref. [37].

Probe	Thermoresistive probes			Thermovoltage-based probes	Thermal expansion based bilayer probes	Fluorescent probes
Thermal sensor/Material	Pt/Rh CNT/Pt	Pd CNT/Pd	Doped silicon	Chromel-alumel Au-Cr Pt-Cr Au-Ni	Al/Si bimetal Al/Au bimetal	Er/Yb codoped fluoride glass
Operation principle	Electrical (resistance)			Electrical (Seebeck effect)	Frequency change/ mechanical deflection	Optical
TCM[a)]	A	A	A	A	A	A
CCM[a)]	A	A	A	A	NA	A[b)]
In liquid application	NA	A	NA	A	Unknown	A
Probe tip radius [nm]	35–2500	25–100	<20	≈10	<20	≈200
Lateral spatial resolution [nm]	6–400	<60	<10	<10	≈0.01	<200
Temperature resolution [mK]	500	12	7	15	Frequency 120 Deflection 0.01	NA
Thermal time constant [µs]	≈200	300	400	≈150	≈3	NA
Thermal sensitivity	NA	0.18 [K µW^{-1}]	2 [µK Hz$^{0.5}$] [c)]	1.06 [K µW^{-1}]	7.1 [mV K^{-1}]	0.5 K^{-1}
Effective sample k range [W m^{-1} K^{-1}] [d)]	0.1–10	1–200	0.1–10	<2400	NA	NA
Maximum operating temperature [°C]	200	160	1000	800	NA	50
Comments	Simultaneous topography and temperature mapping, high resolution, but complicated postanalysis is required			Simultaneous topography and temperature mapping, high resolution, but difficult to fabricate	High temperature resolution, but extremely difficult to fabricate	In liquid mapping, but specialized setup is required
Examples	[1e,18b,23a,31,32,34b,38]			[1b,9c,33a,e,g,h,37,39]	[10b,40]	[20a,35a,b,41]

[a)]A means available, NA means nonavailable or not demonstrated yet; [b)]The CCM is possible for fluorescent probes, e.g., by gluing fluorescent particle on Wollaston wire probe and running current to induce Joule heating[41a]; [c)]This thermal sensitivity is evaluated with respect to time, while others are with respect to measurable electrical signals; [d)]Effective means one equivalent sample thermal conductivity representing all component in the sample setups for example thin film on substrate, suspended thin film and nanowire arrays.

to self-heating effects is passed through the probe. The heat flow from a heated sample to the probe increases the probe temperature and its electrical resistance (R_p) changes, as shown in the following equation

$$R_p(T) = R_{p0}(1 + \mathrm{TCR}(T - T_0)) \tag{1}$$

where $R_p(T)$ is the probe electrical resistance with temperature changing from T_0 to T and R_{p0} is the probe electrical resistance at reference temperature T_0.

Passive-SThM is applied for measuring in-plane temperature profiles in micro/nanoelectronic devices. Its application includes providing a precise localization of "hot spots" in microchips, the regions in which excessive heat generation is generated by the electric current.[43] Passive-SThM could be a useful technique to identify the narrowing of interconnect lines due to fabrication errors or electromigration, while it also provides the diagnosis of on-chip resistive elements.[18a]

Active-SThM: In Active-SThM, the probe is heated up. Direct or indirect methods can be utilized to heat up the probe tip. The direct method employs Joule heating by current flowing through the probe.[1g,9d,38k,l,44] In the indirect method, a separate heater is used to generate heat which is delivered to a tip fabricated from high thermal conductivity (k) materials.[45] In the direct method, an effective Joule heating can be generated in the probe by a larger AC/DC current going along the probe. This method is typically used for thermal property measurement of different materials. The heat flow goes from probe to the sample. The temperature of the probe changes depending on the thermal properties of the sample. The probe temperature rise is monitored from the change of its electrical resistance for thermistor probes, as seen in Equation (1). The experiment can be performed in two conditions: constant-current or constant-temperature probe. In the former mode, the power applied to the probe is kept constant during the experiment while monitoring the change of probe temperature. The latter mode uses a feedback loop to maintain the probe temperature while altering and recording the applied currents during scanning. It is useful to investigate the heat transfer from the sensor tip to the sample due to its dependence on sample local thermal conductivity. Hence, Active-SThM can be applied to characterize the uniformity and novel thermal properties of materials, especially for micro/nanoelectronic systems.[1i]

In active mode, the sample can also be locally heated to investigate thermal properties including SJEM, dynamic localized thermomechanical analysis method,[46] to locally melt the sample or for nanolithography.[47]

DC and AC Heating SThM Operation: Heating and sensing with the thermistor probe can be performed by DC, AC or a combination of AC and DC modes.[18a] In most Active-SThM, just DC current is enough to heat the probe. Analytical heat transfer modeling of DC probe heating is a useful method for quickly reducing and easily interpreting experimental data.[48] However, the more advanced AC mode provides opportunities

© 2019 The Authors. Published by WILEY-VCH Verlag GmbH & Co. KGaA, Weinheim

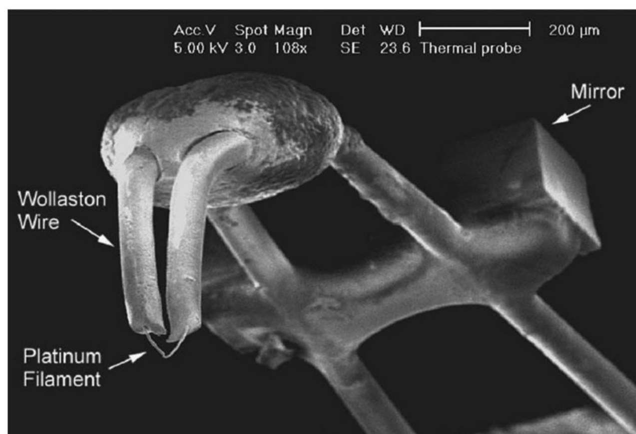

Figure 2. A Wollaston probe imaged under scanning electron microscope (SEM). Reproduced with permission.[58] Copyright 2011, Scientific Research Publishing.

for lock-in measurements with high signal-to-noise ratio[49] and the combination of AC and DC might provide more stable measurements for high-current heated samples.[13] For example Gomès et al.[50] sensed temperature rise of AC heated integrated circuits by DC powered Wollaston wire probes.

Active-SThM Using 3ω Method: A special active-SThM method combined with the 3ω method (3ω-SThM) is briefly described here. In short, when AC current with frequency ω is applied on a resistor, a Joule heating component occurs at the second harmonic frequency 2ω leading to a resistance alternation at 2ω. The voltage drop across the resistor equals the product of resistance at 2ω and applied current at ω, having a measurable 3ω component that is directly proportional to the AC temperature of the resistor.[47b] The 3ω method was originally applied to heaters micropatterned on bulk and film on substrate samples[51] and is quite popular owing to its controllable heat delivery and high signal-to-noise ratio.[47b] The 3ω signal can be measured by a lock-in amplifier along with a Wheatstone bridge circuit.[48b,49,52] The 3ω-SThM can be used for mapping temperature and thermal conductivity.[44c,53]

2.2.2. Wollaston Wire Probes

The very first resistive based thermal probe was designed by Pylkki et al.,[31,54] shown in **Figure 2**. Its development benefited from the thin wire drawing technique proposed by Wollaston et al.[55] The drawing technique provides a 5 µm diameter Pt90/Rd10 coated with a 70–75 µm silver shell. The wire was bent into a U-shape cantilever, then the V-shaped tip was electrochemically etched to expose a 200 µm segment of the platinum alloy core as the resistive element of the probe. An aluminum tape was attached to the cantilever as a mirror that reflects a laser beam onto a photodetector. The probe characteristics were documented as ≈5 N m^{-1} cantilever spring constant, TCR of 0.00166 K^{-1}, and time constant of 200 µs.[52b,56] Achieving a 0.5 µm lateral spatial resolution at that time was a breakthrough of diffraction limited resolution of optical methods as well as enabling scanning across nonconductive sample surface, which was not possible by STM. Wollaston wire probes had major contributions on thermal

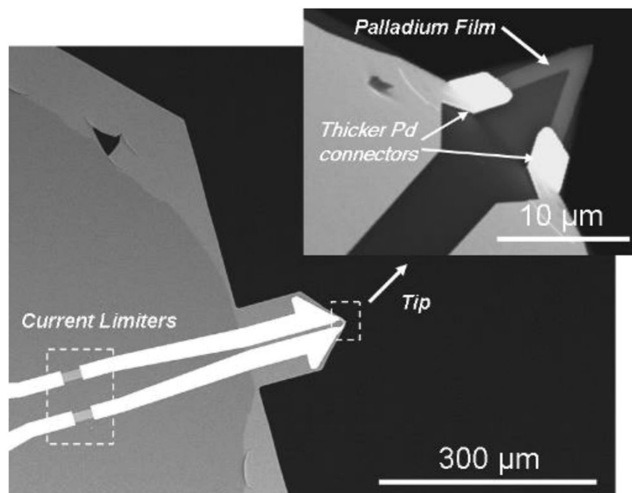

Figure 3. SEM image of Pd on SiO_2 probe. Reproduced with permission.[60] Copyright 2011, American Institute of Physics.

contact investigations between probe and sample.[9b,47b,57] However, its limitations were also apparent. The spatial resolution was far from nanoscale and the fabrication process was difficult to adapt for batch fabrication, with significant variations between each probe, making probe characterization a necessary step before SThM experiments.[24] Therefore, the paths for improving the spatial resolution and the ease of fabrication of resistive thermal probes inspired from Wollaston wire probe went two ways. One was making smaller probes or attaching materials on tips with smaller sizes, for example a diamond attached Wollaston probe,[45] or a cantilever with a complete Pt probe by mic rofabrication.[34b,c] Another path was distributing a large aspect ratio thermoresistor on a materially heterogeneous support to assure unidirectional heat flow to sample, such as Pd or nickel chromium (NiCr) thin film probe and CNT probe.[1e]

2.2.3. Probes of Shrinking Size

Downsizing the Pt or NiCr thermoresistor by batch micro or nanofabrication, specifically through a series of low pressure chemical vapor deposition (CVD), micromachining, and electron beam lithography[33g] on 500 nm thick Si_3N_4, enabled a 100 nm spatial resolution thermistor probe as the tip dimension reached nanoscale,[59] as shown in **Figure 3**.[60] Commercial probes with Pd as core element, known as Kelvin nanotechnology (KNT) probes achieved sub-100 nm spatial resolution and 0.1 K temperature resolution.[61] Basic specifications were 0.35 Nm^{-1} spring constant, TCR of 0.0012–0.0016 K^{-162}, and ≈5 ms per point time response.[38f,63] However, the probe design also brings a thermally induced cantilever deflection artifact caused by thermal expansion in different probe-cantilever materials. When SThM operated with a feedback loop that maintained constant force or distance just like AFM, this false cantilever deflection would disturb experimental performances for both active and passive operating modes and might generate inaccurate results, even damage the probes. Zhang et al.[63] revised the probe and cantilever design to compensate for this

© 2019 The Authors. Published by WILEY-VCH Verlag GmbH & Co. KGaA, Weinheim

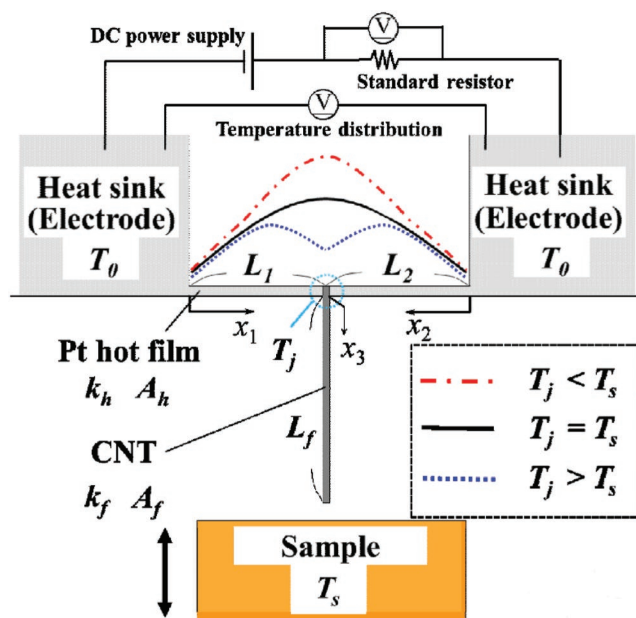

Figure 4. Heat transport mechanism of a suspended Pt film with CNT probe. Reproduced with permission.[38c] Copyright 2013, Elsevier B.V.

thermally induced cantilever deflection by a metallization groove that provided a mechanical balance and similar spring constant.

A Pt thin film was also used as heat source by Hirotani's group to develop the CNT probe.[38c] CNTs are well known for high thermal conductivity, outstanding hardness, durability, and nanoscale tip radius (≈50 nm). A cylindrically rolled carbon sheet of sp^2 hybridization was attached from a suspended Pt thin film shown in **Figure 4**. The Pt thin film controls heat flux and quantitatively determines surface temperature by a methodology similar to what was introduced in null-point SThM (NP-SThM) described in Section 4.5.1.[64] The sample temperature was deduced from 1D heat conduction equation seen in ref. [38c].

A recently proposed batch-fabricated nanoscale probe using a focus ion beam (FIB) method produces an integrated piezoresistive force sensor with the SThM probe that allows operation without the need of the photodetector instrumentation in SThM.[38i,q] For thermal sensing, a Pt or Cr/Au thin metal filament was deposited on/grown from a silicon cantilever by a modified FIB method after consecutive lithography and chemical etching processes defined the rest of the probe. An scanning electron microscope (SEM) image of the piezoresistive probe is shown in **Figure 5**.[38q] The thermal resistor, Wheatstone bridge, and piezoresistive sensors were all integrated on the probe. The deflection of the cantilever would be detected by the resistance change of the piezoresistive sensor. Discarding the photodetector and laser emitter was advantageous for operating SThM in vacuum environment.[9d,37,65] This helped to precisely control the cyclic load force that prevents probe deterioration and sample surface damage, and for eliminating the induced thermal drift of the probe signal with 37% reduction in the maximum measurement error.[66] High piezoresistive deflection (257 μV nm^{-1}) sensitivity, probe sensitivity, and ease of calibration using the double scan[39f] along with sub-100 nm tip radius empowered nanoscale temperature quantification and localized heat generation.[67]

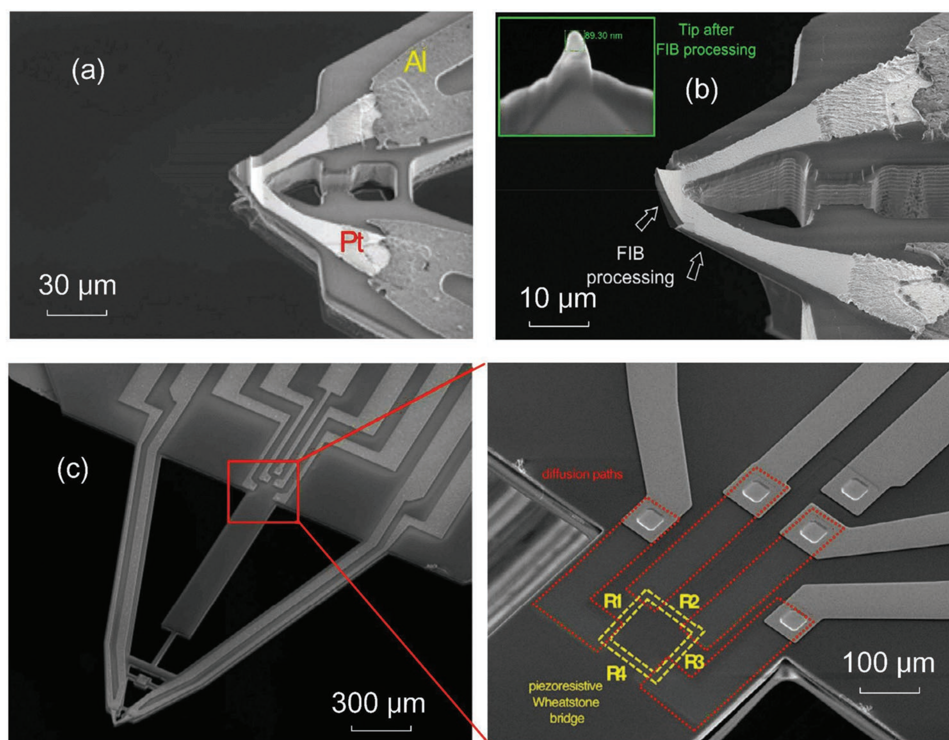

Figure 5. SEM images of piezoresistive probes. a) Al-Pt probe tip. b) SThM cantilever. c) Cantilever with a zoomed in of the Wheatstone bridge. Reproduced with permission.[38q] Copyright 2018, Elsevier B.V.

© 2019 The Authors. Published by WILEY-VCH Verlag GmbH & Co. KGaA, Weinheim

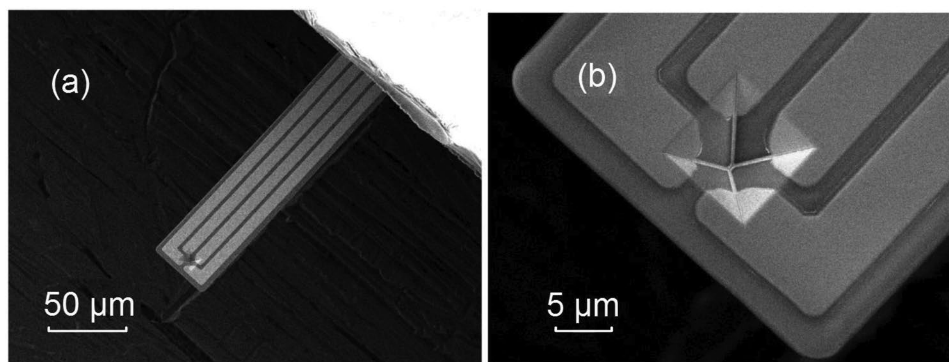

Figure 6. SEM image of the top view of the probe that includes a SiN_x cantilever and a sharp Pt wire tip. A four-terminal thermal element sits directly above the pyramidal tip apex. Reproduced with permission.[68] Copyright 2014, Institute of Physics (IOP) Science.

Another fabrication strategy was proposed by Hatakeyama et al.[68] to facilitate low-cost massive probe manufacturing. **Figure 6** shows an SEM image of this probe. It consists of a four-terminal gold on AFM cantilever supported by a glass holder on bulk silicon with a 100 nm Pt pyramid tip, which was produced with conventional contact lithography and micromachining.

2.2.4. Doped Semiconductor Resistor Probes (DS Probe)

A special category of thermoresistive probes is doped semiconductor (DS) resistor probes and heaters. Silicon nanoprobes were originally developed for the Millipede device International Business Machines Corporation (IBM)[44d] for data-storage devices and high-speed nanolithography,[69] and then the probe design was used in SThM setups to measure sample temperature.[9d] This kind of U-shaped cantilever consists of a high doped semiconductor region as the cantilever and the low doped tip region as the sensor. A conical tip with ≈10 nm curvature radius and micrometric height was fabricated on top of the lower doped resistive element. Nelson and King[38j] designed the silicon probes with pyramidal tips as illustrated in **Figure 7**. It is noted that additional information is required for the variation of the electrical resistance versus temperature because of their nonlinear relationship. Further enhancement of DS probe performance includes improved thermal insulation,[70] additional Pt layer to enable thermovoltage measurement,[71] and multimatrices of microcantilevers.[38o,72] A review of its applications and some examples are given in ref. [47a].

In summary, the main advantages of thermoresistive probes are that no specialized devices are needed, just simple DC/AC-currents and/or Wheatstone bridges are enough to measure accurate results. In addition, it is very easy to use them as a heat source. For example, an SThM probe with a resistive Si heater can be used to precisely lithograph the surface in nanoscale.[73]

2.3. Thermovoltage-Based Probes

SThM thermometry can be based on thermovoltage generated at the joint between two dissimilar electrodes due to thermoelectric effects.[29,30] Thermoelectric junctions can be built between the sample surface and the tip in noncontact such as in the tunneling thermometry[34d,54,74] or by a point contact thermocouple formed between the probe and sample.[75] Both methods require a conductive sample surface or a conductive coating being applied on samples, thus applications are limited. More versatile thermovoltage methods include the use of thermocouples at the probe tip using the Seebeck effect.[18a] The history of this method can traced back to 1986,[29] but its purpose was not mainly for temperature profiling and required the samples to be conducting. Majumdar et al.[30] developed the wire thermocouple AFM probe which could be applied with nonconducting and conducting samples. However, the signal was strongly disturbed because it was dominated by air conduction between probe tip and sample. Later methods to mitigate air conduction influence were developed by Shi et al.[1b] and Luo et al.[33b,e] by reducing the thermocouple junction size and replacing the wire thermocouple by a thin film with lower thermal conductivity, respectively. Thin film thermocouple probes were further optimized by a nanofabrication method developed by Weaver and co-workers.[33g,76] Further size reduction of the probe thermocouple including the wire junction tip and cantilever not only enhance the spatial resolution due to a

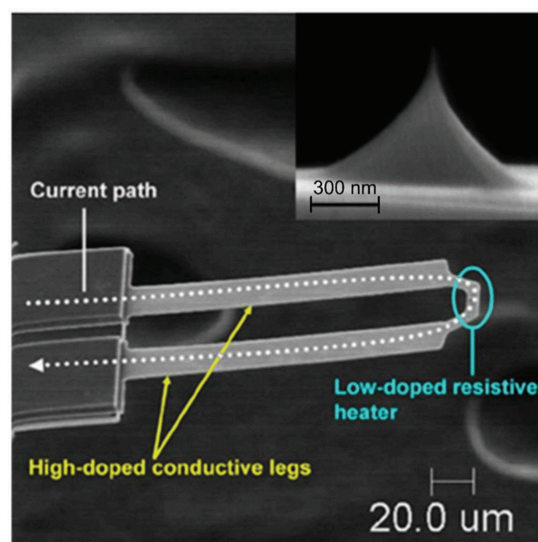

Figure 7. SEM images of the cantilever and the tip (inset figure) of DS probes. Reproduced with permission.[38j] Copyright 2007, American Institute of Physics.

© 2019 The Authors. Published by WILEY-VCH Verlag GmbH & Co. KGaA, Weinheim

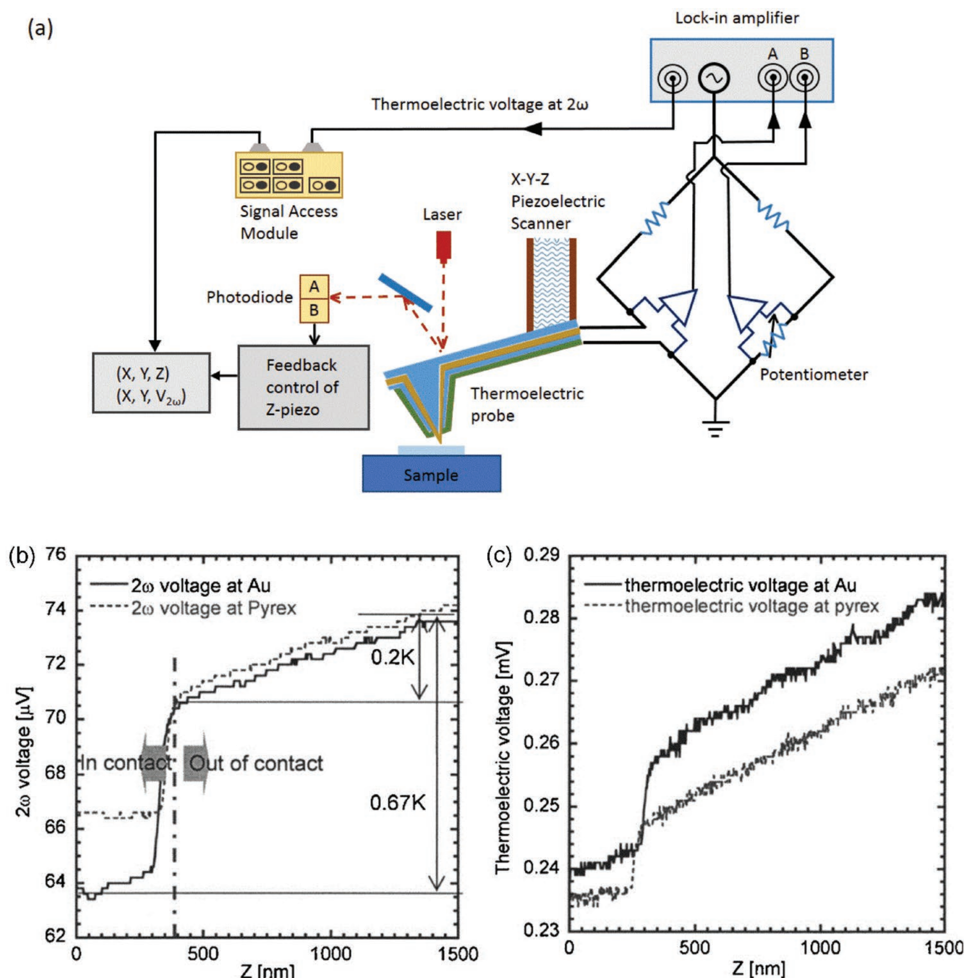

Figure 8. The 2ω technique. a) Schematic diagram of 2ω techniques with thermocouple junctions with AC currents. b) 2ω probe signal as a function of probe tip–sample separation. c) Thermoelectric voltage as a function of tip-probe distance. Adapted with permission.[39d] Copyright 2006, American Institute of Physics.

smaller tip radius but also significantly improve time response due to a smaller heat capacity.[2,33g,76a,77]

Active-SThM thermocouple mapping of thermal conductivity was first proposed by Oesterschulze et al.[78] in which a coaxial thermocouple mounted on STM was heated by an external laser-beam. Roh et al.[39d] powered the thermocouple probes with an AC current of angular frequency ω to measure thermal conductivity with higher spatial resolution. The alternative temperature of the heated thermocouple at 2ω was directly measured by the induced Seebeck voltage. This method is believed to have several advantages than the thermoresistor probe. First, the heating is localized at the very tip of the probe and second, using the low-thermal conductivity material for the cantilever results in a good thermal insulation of the probe tip. To test this method, Roh et al.[39d] scanned a gold wire with 2ω, 3ω, and DC laser heating. It was found that the 2ω signal was able to distinguish between the thermal properties of the gold heaters and Pyrex glass, as shown in **Figure 8**, while the contrast disappeared when using 3ω mode. This is due to averaging along the probe in 3ω mode, which is not sensitive in this setup. Thiery et al.[79] investigated the thermal contact conductance (0.6–10 μW K^{-1}) of different thermocouple dimensions and contact materials in active mode.

Later, Kim's group developed the double scan method[39f] and NP-SThM[64] with thermocouple probe junctions. More recently, Kim et al.[37] used SThM implemented in ultrahigh vacuum (UHV), which has the capability of quantitatively mapping temperature fields with high spatial resolution for thermocouple-based probes. Bontempi et al.[80] attached an S-type thermocouple on the quartz tuning fork (QTF) shown in **Figure 9** to replace the optical deflection detection unit of SThM, where shift of natural frequency of QTF could indicate the moment of contact.

Although the predecessor of KNT probe (Pd based thermoresistive probe) was based on thermovoltage methods, the thermocouple probe has not been commercially produced.[32,33g] For both the thermocouple probes and thermoresistive probes, one of the major issues of temperature measurement is the cooling effect occurring between the probe and the sample that is measured. In this scenario, the sample temperature may be affected by the measurement. Moreover, the measured

© 2019 The Authors. Published by WILEY-VCH Verlag GmbH & Co. KGaA, Weinheim

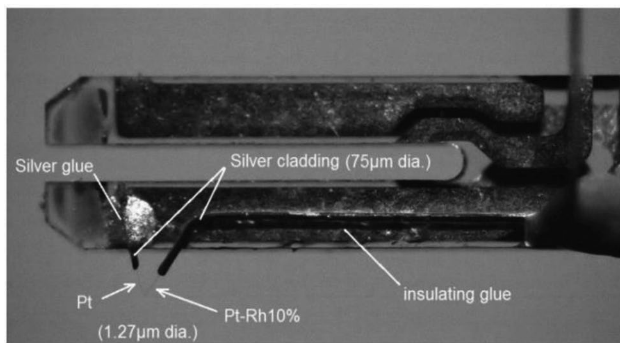

Figure 9. Thermocouple probe integrated on a quartz tuning fork (QTF). The arrows point out to the thermocouple junction, which is made of Pt and Pt-Rh10% wires with a tip diameter of ≈1.27 µm. Reproduced with permission.[80] Copyright 2016, American Institute of Physics.

temperature from the probe is considered many times as the true sample temperature. However, this approximation is not accurate due to the presence of the thermal contact resistance (thermal exchange resistance) between the probe and the sample surface,[1b] which will be explained in Section 3 and 4. Several calibration methods have been proposed to take this into account, for example the NP method[64] (Section 4.5.1) for temperature sensing and intersection methods[7a] (Section 4.5.2) for thermal conductivity measurement. This discrepancy between the sample temperature and the tip temperature should be carefully considered but it is often neglected in SThM.[10c]

2.4. Other Types of SThM Probes

One major issue for thermoelectric and thermoresistive probes is that if the sample material is electrically conductive, probes may change the state of the sample when operating in contact mode.[24] Also it is hard for these types of probes to be used in liquid environment because strong electrical conductivity of liquid leads to distorted probe signals.[24] Thermal expansion based bilayer probes and fluorescent probes could solve these problems. In addition, a few other thermal effects can be implemented in the development of new SThM probes.

2.4.1. Thermal Expansion Based Bilayer Probes

Thermal expansion based cantilevers and probes are composed of two thin films sandwiched on top of each other and benefited from the thermal expansion difference of dissimilar materials. The significantly different thermal expansion coefficient between the top and bottom materials causes a temperature dependent deflection of the cantilever. First in 1994, bilayer microcantilevers made of Si-Al materials were selected by IBM to measure the solution temperature in several chemical reactions.[81] In the next year, Majumdar's group used the similar kind of probes to scan sample surfaces.[36] Recently, a bilayer subcantilever was fabricated at the tip of a standardized cantilever using FIB.[38d] It is stated that this operation can guarantee to synchronously record the surface topography and temperature through the detection of the deflection at two distinctive frequencies. This kind of approach is helpful in noncontact Passive-SThM but the resolution needs to be improved. The same principle of thermal expansion induced cantilever deformation was tweaked by McConney et al.[10b] who demonstrated an asymmetrical bimorph thermal probe that produced lateral deflection. The method was named scanning thermal twisting microscopy (STTM) that uses a tip with a radius of 5 nm and achieves a temperature resolution of few mK. The working principle and a comparison of STTM with normal bilayer cantilever are shown in **Figure 10**.

2.4.2. Fluorescent SThM Probes

The photointensity ratio between two adjacent fluorescent nanoparticles or nanoribbons is temperature dependent. Based on this principle, researchers glued erbium ion doped fluoride material on traditional AFM probes and developed a novel SThM probe for temperature sensing.[35a,b,41a,b] A recent investigation reported that the Er^{3+}/Yb^{3+} fluorescent nanocrystal glued on the top of a tip has high and low intensity peaks at 540 and 520 nm wavelength, respectively.[41c] The SEM of a fluorescent probe is shown in **Figure 11**.[82] The temperature can be then calculated from the following equation

$$I_{520}/I_{550} = Ae^{-B/T_s} \tag{2}$$

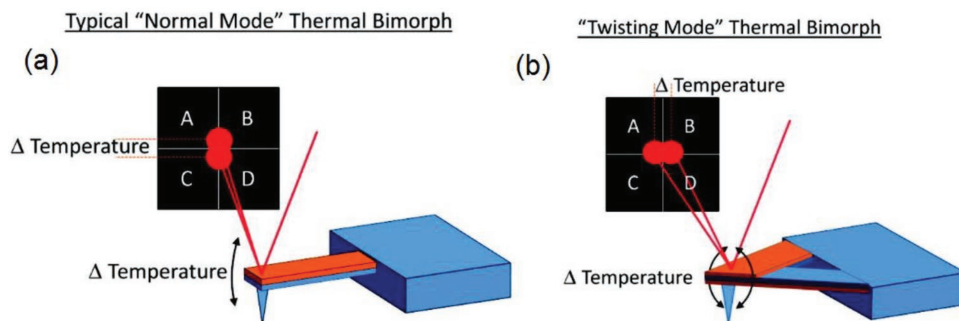

Figure 10. Schematic diagram of the deflecting motion of a typical thermal bimorph. a) Normal mode is the vertical deflection of cantilever due to temperature change. b) Twisting mode is the angular displacement due to temperature change. Reproduced with permission.[10b] Copyright 2012, American Chemical Society.

© 2019 The Authors. Published by WILEY-VCH Verlag GmbH & Co. KGaA, Weinheim

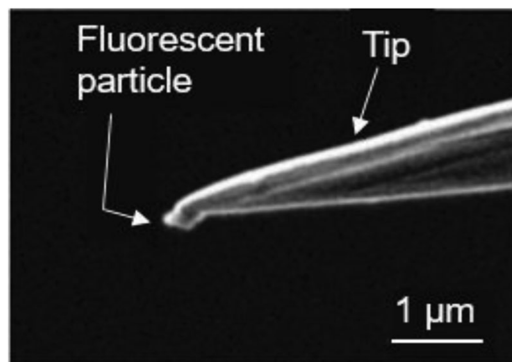

Figure 11. SEM images of fluorescent nanocrystal glued onto a tip. Reproduced with permission.[82] Copyright 2012, Springer Nature.

where I_{520} and I_{540} denotes intensities at the two wavelengths, T_s is sample temperature, A and B are calibration parameters. A self-heated Pt nanowire was scanned with this tip, and a spatial resolution of less than 200 nm was demonstrated in ref. [41c]. The other advantage of fluorescent SThM probes is that they were able to operate under liquid environment thanks to the strong penetration ability of light.[20a]

2.4.3. Superconducting Quantum Interference Device (SQUID)

From Halbertal et al.[83] this superconducting junction probe shown in **Figure 12** utilized the temperature dependence of critical current in superconducting matters. The authors chose a Pb superconducting junction, also called Pb SQUID, as the probe tip with 23 nm tip radius. The thermometer SQUID on tip (tSOT) was able to perform noncontact scanning to sense power dissipation as small as 40 fW in Nanoelectronics with spatial resolution down to 400 nm and less than 1 µK Hz^{-1} temperature sensitivity. The results from this group revealed the strong potential of this probe, opening up new possibilities for exploration of quantum effects such as Nernst effect[84] using tSOT.

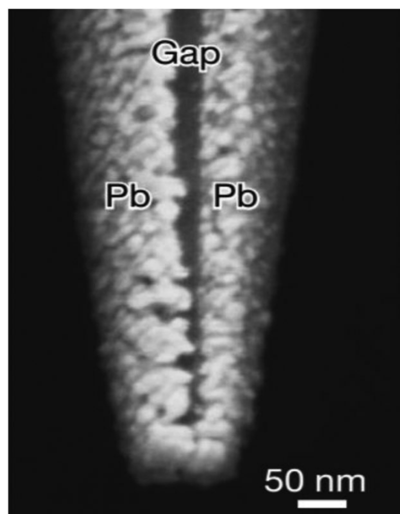

Figure 12. SEM images of Pb superconducting junction. Reproduced with permission.[83] Copyright 2016, Springer Nature.

2.5. Thermoacoustic Effect

Majumdar et al.[2,85] proposed a SJEM in the 1990s to measure material dilation caused by a sample integrated resistive heater. A standard AFM was used to localize the sample surface heated by Joule heating. With a thermal expansion coefficient nearly 10^{-5} mK^{-1}, the minimal dimension of sample needs to be a few tens of micrometers enabling the probe to detect the thermally expanded sample. Cretin et al.[86] selected a similar technique for directly modeling both thermal and thermoelastic fields by finite element analysis (FEA). It is worth noting that knowing the geometry of the sample is required before the experiments starts. In AFM-IR spectroscopy (AFM-IR)[56b] an IR pulse is applied by a pulsed source apparatus[56b] or more practical a table-top IR source.[87] For such process, the sample absorbs radiation that can be detected and analyzed according to the excitation frequency or frequency bands. The thermal expansion phenomenon resulting from the short IR pulse heating makes the AFM tip unsteadily in contact with the illuminated sample, and the cantilever then begins oscillating. The signal is amplified when the heating frequency approaches the cantilever natural frequency thus the resonance of cantilever can be used to filter frequency response. Such a technique can be used for spectroscopic analysis of the sample or to perform spectroscopy involving heating. It has extensive applications in biology, such as for detecting virus location in cells.[88]

2.6. Measurement Devices

2.6.1. Measurement Bridges

To accurately capture the electrical signal and minimize the noise-to-signal ratio, measurement bridges are introduced and widely used today. There are four major types of instrumentations with different specializations and limitations. The classical Wheatstone bridge (**Figure 13**a) is widely used for thermal resistance measurements and was first developed over a century ago.[32,89] Four resistors, including the variable resistance probe, and a potentiometer are used for pre-experiment compensation are needed to operate the SThM system. However, the main disadvantage is that it cannot be applied to a four-contact probe arrangement, which would provide more accurate probe resistance measurements. The transformer-isolated Wheatstone bridge (Figure 13b) was developed to reduce the electrostatic force between the probe tip and sample, which has great advantage when measuring micro and nanoelectronic devices.[32] The Kelvin bridge (Figure 13c) was proposed originally to measure low resistances,[90] where the resistor requires a multiple-point contact, but low sensitivity and high noise was reported on SThM.[22] In order to solve this problem, the Modified Wheatstone Bridge was designed by the replacement of the regular voltage difference measurement with that of the amplified probe voltage (Figure 13d). It is shown that

© 2019 The Authors. Published by WILEY-VCH Verlag GmbH & Co. KGaA, Weinheim

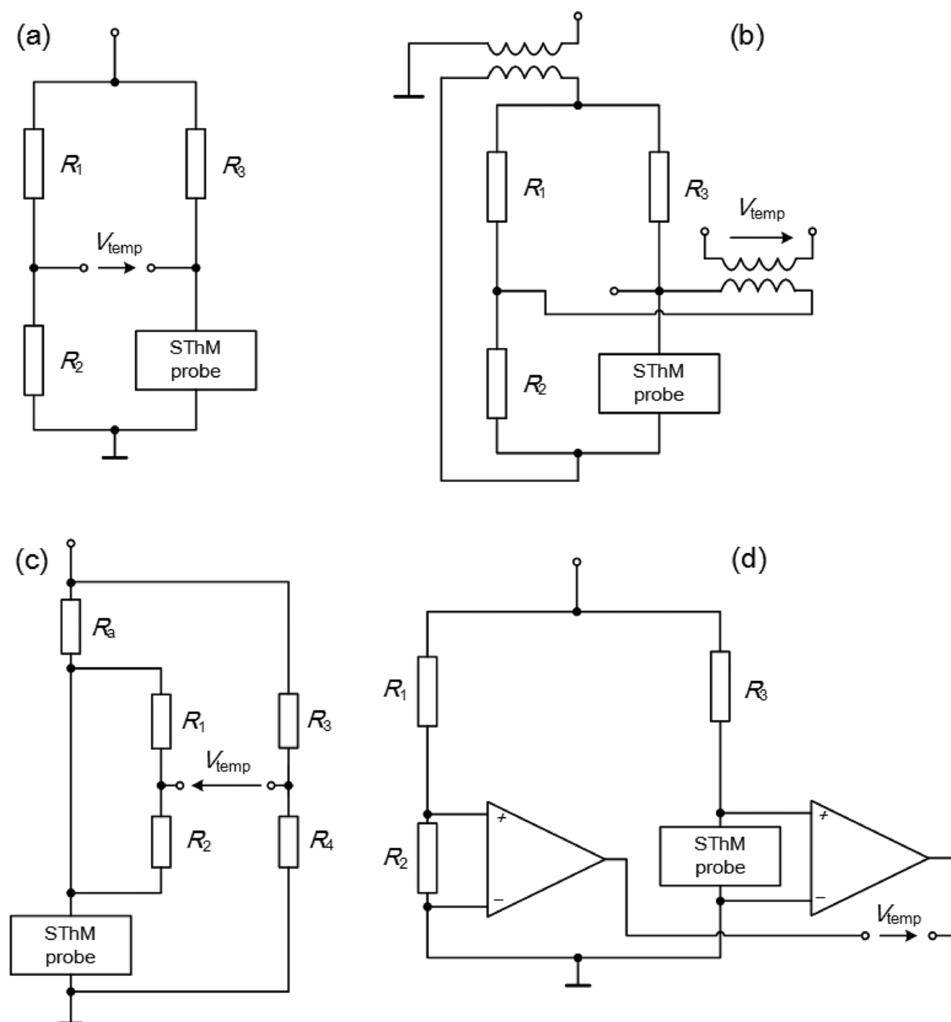

Figure 13. Schematics of SThM measurement bridges. a) Wheatstone bridge, b) transformer-isolated Wheatstone bridge, c) Kelvin bridge, and d) modified Wheatstone bridge. Reproduced with permission.[24] Copyright 2015, Elsevier.

the modified version has higher measurement sensitivity than Kelvin bridges and the standard Wheatstone.[38l]

2.6.2. Supporting Cantilevers

Micro cantilevers act as probe holders, heat sinks, force loaders, and contact indicators in SThM, similar to a typical AFM cantilever. The most common cantilevers are reflectors combined with a laser-photodetector unit, with some exceptions of novel integrated cantilevers, such as heated AFM cantilevers.[47a] Other potential cantilevers are aforementioned piezoresistive cantilever whereby its deflection was converted to resistance change of the piezoresistive sensor integrated in the cantilever along with other microcircuits.[38i,q] Another interesting idea of cantilever utilizes the mechanical dependence of natural frequency change of QTF as mentioned above.[80] Overall, recognizing the importance cantilevers play in thermal management of SThM system is imperative for proper cantilever selection or design optimization in the future.

2.7. SThM System Setup

The SThM can be operated in atmospheric conditions, as a standard AFM mode, using the configurations explained in Section 2.6 and some of the probes described in Section 2.5. However, there are other possible measurement setups as explained in this section.

2.7.1. Ultrahigh Vacuum-Based Scanning Thermal Microscopy (UHV-SThM)

To remove the parasitic heat transfer by air and liquid meniscus between probe and sample and to improve the spatial resolution of SThM, an UHV-SThM system operating in an ultrahigh vacuum environment was established.[37,65] Hinz et al.[65] first proposed the quantitative UHV-SThM and Menges et al.[9d] used heated tip probes to make quantitative temperature sensing in vacuum. Then, this technique was successfully employed for quantitative nanoscale thermometry with high

© 2019 The Authors. Published by WILEY-VCH Verlag GmbH & Co. KGaA, Weinheim

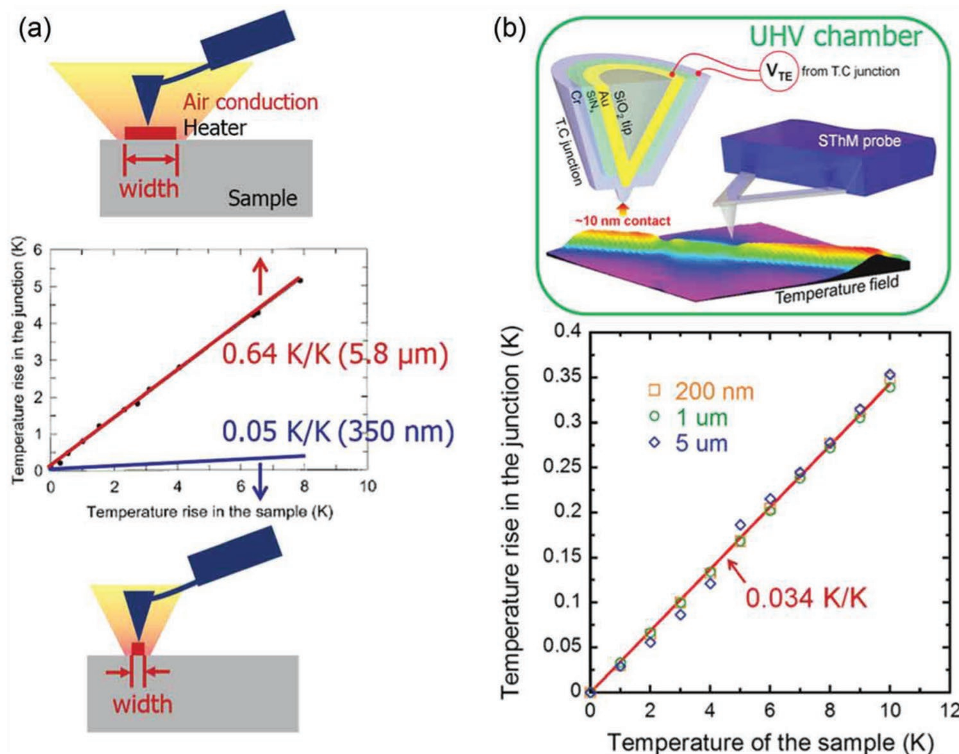

Figure 14. Measurement of SThM sensitivity in different environments. a) Temperature rise, i.e., tip sensitivity, in the thermocouple tip due to two different sample heater areas (blue line: 350 nm heater width, red line: 5.8 μm heater width) measured in air, b) Sensitivity of a thermocouple tip versus temperature of the sample measured in UHV chamber showing no dependence with the heater dimensions, e.g. heater line's width from 5 μm to 200 nm. a) Reproduced with permission.[9a] Copyright 2015, Taylor & Francis. b) Reproduced with permission.[37] Copyright 2012, American Chemical Society.

temperature resolution (≈15 mK) and sub-10 nm spatial resolution.[37] **Figure 14** shows the probe sensitivity when surrounded by ultrahigh vacuum. While ref. [9a] shows that in air the sensitivity is highly dependent on the heated areas, however, in a UHV chamber (Figure 14), the sensitivity is almost unchanged for different heating areas. The dependence of sensitivity to heated area sizes might come from the contribution of the air mediated thermal transport, which indicates nonlocal temperature measurement. Further, the size of the liquid meniscus contributing to the thermal resistance might also limit the resolution of SThM.

To take advantage of near-field thermal radiation in UHV, an SThM operating within an STM has been developed by Kittel et al.[10a,77,91] A thermocouple-based probe is fitted at the very end of the tip and the device is positioned in a vacuum environment. In noncontact mode and in vacuum the setup is capable to perform near-field radiation measurements between the very tip and the sample. Examples include the detection of heat radiation from a thin film dielectric material by near-field SThM.[92] UHV is an ideal environment to eliminate uncertainties of multichannel heat transfer between tip and sample dominated either by solid-solid contact in contact mode or by radiation in noncontact mode. However, there are some limitations on UHV such as i) biological samples and other pressure sensitive samples are difficult to measure under UHV, ii) the expense of operating UHV is high and operation is difficult, and iii) in noncontact UHV, the signal from radiative heat transfer has large uncertainty and it is hard to conduct postanalysis. Alternatively, the noncontact in ambient condition is advantageous. It eliminates solid–solid heat transfer, operates without expensive setups, and it can measure any type of samples.

2.7.2. Liquid-Based Scanning Thermal Microscopy (i-SThM)

To extend the opportunities for SThM in biological materials, energy regeneration devices, and catalysts, the liquid immersion SThM (i-SThM) was first proposed by Aigouy et al.[35a] The principle to scan in liquid environment was to use fluorescent probes (Section 2.4.2) that monitor the optical intensity of the attached fluorescent particle. Tovee et al.[21,38r] later proposed a KNT probe was also feasible to operate in liquid environment as i-SThM. Its spatial resolution, around 30 nm, and thermal sensitivity measured by i-SThM is below that in the air. The authors found that liquid immersion SThM can make very stable thermal contact between the probe tip and the sample, removing the expensive UHV devices and the major disadvantages of ambient environment.[21]

2.7.3. SThM Combined with Shear Force (FS)

By laterally moving the probe when in contact with the sample, both the normal force and the lateral shear force can be measured by cantilever deflection while the thermal resistance is

© 2019 The Authors. Published by WILEY-VCH Verlag GmbH & Co. KGaA, Weinheim

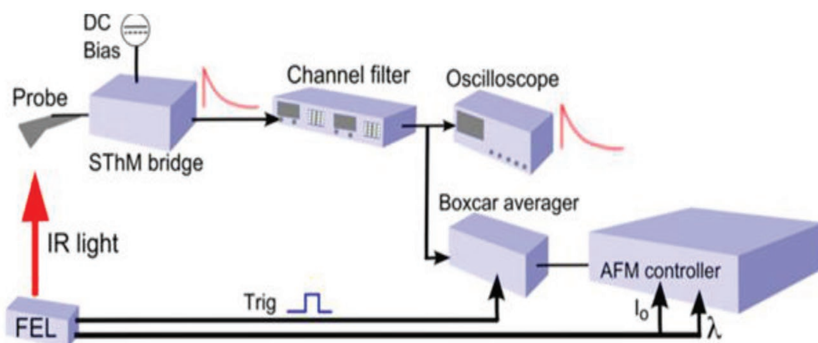

Figure 15. SThM-IR experimental instrumentation for ALICE IR laser, where I_0 is the current directly related to the IR intensity. Reproduced with permission.[42] Copyright 2015, IOP Science.

measured through probe tip. Since the shear force and the thermal exchange parameters depend on contact area, FS-SThM unearth the nanoscale heat transport through solid contact between diffusive and ballistic regime.[93] However, FS-SThM strictly requires careful monitoring of synchronized probe holder and sample temperature such that the thermal response variation with time is minimized. Another source of uncertainty comes from the laser used to monitor the cantilever deflection, since it may disturb the probe temperature.[94]

2.7.4. SThM Combined with IR Spectroscopy

Spatial resolution of far field infrared spectroscopy is limited by laser's diffraction wavelength. An alternative route is to use IR heating to induce a local temperature difference on probe or sample. When IR heats the sample, SThM can be used to measure the temperature rise that correlates to the IR absorption of the sample[95] as seen in **Figure 15**. On the other hand, when the probe is heated the setup can be used to measure the sample thermal conductivity. In the former case, however, the SThM signal is strongly interrupted by direct probe heating inducing background signals.[42]

Quantitative SThM usually has limited scanning area. When it is combined with IR spectroscopy's large scanning range, the general high temperature region could be easily located by IR spectroscopy and then exact hot spot location could be detected by SThM.[96] The outcome will have high resolution results over a large area that is desirable in hot spot detection in microelectronics.

3. Heat Transfer Mechanisms

The spatial resolution and sensitivity of SThM techniques are highly dependent on the heat transfer mechanisms between the thermal sensor and the sample. The thermal exchange resistance between the probe and sample can be summarized in the following equation assuming that the heat transfer mechanisms are independent.[1b,2]

$$\frac{1}{R_c^{th}} = \frac{1}{R_{ss}^{th}} + \frac{1}{R_{air}^{th}} + \frac{1}{R_w^{th}} + \frac{1}{R_{rad}^{th}} \tag{3}$$

where R_c^{th} is the effective thermal exchange resistance including the heat transfer by tip–sample contact conduction, R_{ss}^{th}, surrounding air gap conduction, R_{air}^{th}, water meniscus conduction, R_w^{th} and radiation, R_{rad}^{th}. The thermal interaction between the probe tip and sample are in fact more complicated than what Equation (3) depicts since additional thermal resistance occurs across heat transfer channels due to their distinctive temperature gradients. The assumption of independent heat fluxes is a simplification of the multidimensional heat transport behavior, where its validity and significance could be addressed in the future.

Figure 16a shows a schematic diagram of heat transfer resistance/path of the whole SThM system in the active (left side) and passive mode (right side). Figure 16b shows the detailed heat transfer mechanisms between the probe and sample in active mode, which can be also applied to the Passive-SThM when the heat flows in the reverse direction.

3.1. Air Conduction

If SThM measurements are not carried out in a vacuum environment, the air conduction around probe and sample becomes important. The effective heat transfer coefficient between probe and surrounding air h_{eff} and also the air gap thermal conductance G_{air} between the probe and the sample must be taken into account. **Table 2** summarizes the h_{eff} and G_{air} as obtained experimentally and numerically.[9d,38e]

When the probe works in noncontact mode and the distance between the tip and sample is larger than the air MFP, Fourier's law describes heat transfer through the air gap. However, if measurements are performed in contact mode or noncontact mode, and the distance between probe surface and sample surface in certain regions of the probes is smaller than air MFP then the ballistic regime should be considered. This means that the continuum assumption is not appropriate in the tip region and Fourier's law cannot be used. Thus, some methods have been provided to solve this problem. One approach uses an effective thermal conductivity to replace the bulk thermal conductivity of the air. This method was first provided by Shi et al.[1b] who fully described the air conduction between the probe and the sample. The h_{eff} deduced from the effective air thermal conductivity in 1D heat transfer model can be expressed by the following equation

$$h_{eff}(x) = \frac{k_{air}}{\delta(x)} \tag{4}$$

where k_{air} is the effective thermal conductivity of air, $\delta(x)$ is the tip–sample distance, and x is the coordinate along the probe. Several investigations take the relationship between k_{air}, temperature, and MFP into account to obtain the h_{eff}.[33f,100] More accurate but complex methods such as direct simulation Monte Carlo[101] and a quasi-ballistic heat transfer model[102] were developed to evaluate the subcontinuum conduction.

© 2019 The Authors. Published by WILEY-VCH Verlag GmbH & Co. KGaA, Weinheim

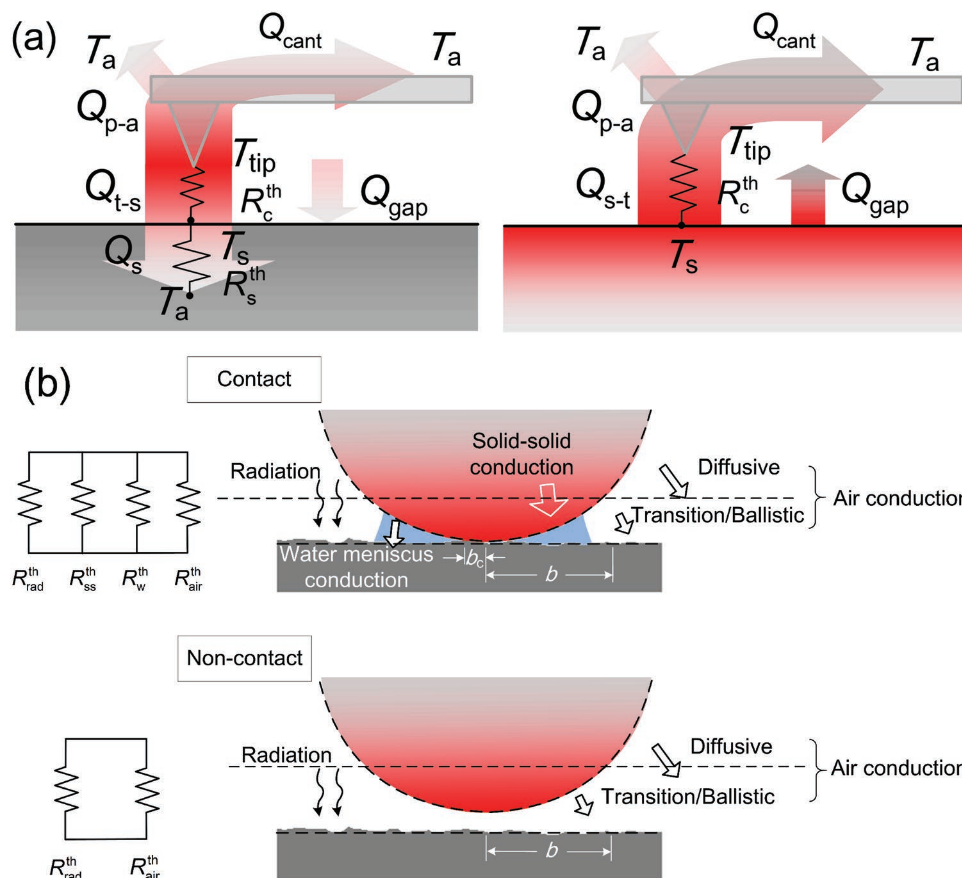

Figure 16. a) The heat flow diagram of probe–sample system and thermal resistance network in the active and passive modes with b) zoom-in at the probe–sample interface identifying the different heat transfer mechanisms involved in the contact and noncontact modes. Adapted with permission.[10c] Copyright 2015, Physica Status Solidi (a).

3.2. Water Meniscus

When the probe tip contacts the sample surface in humid air or atmospheric conditions, a water meniscus is formed between the tip and the sample. As a consequence, the heat also transfers across this water meniscus. Majumdar's group[33b] first suggested the dominance of water meniscus conduction among heat transfer mechanisms of probes with thermocouple tips based on the Kelvin Equation (5)

$$G_w \approx 2\pi k_w S_s \tag{5}$$

where G_w is thermal conductance through water meniscus, k_w, is the meniscus thermal conductivity, and S_s is a shape factor as the function of tip–sample separation, meniscus width and angle of apex occupied by meniscus. However, in this work the authors did not consider the thermal resistances of probe-water and water-sample contacts. Shi et al.[1b] then revised and proposed that the interface resistances between the water meniscus and the probe tip can be significant and comparable to that of air conduction. Assy et al.[103] also took these thermal resistances into account and pointed out that G_w does not dominate probe–sample interaction of Wollaston wire probes at any temperature in active mode. The reason is that the water meniscus thermal conductance is larger than 0.2 μW K^{-1}, which is much smaller than that of air conduction.[47b,57] The research shows that the water meniscus can be calculated through the capillary forces for various Wollaston probes. Afterward, Assy et al.[38a] investigated the temperature dependent capillary forces in nanoscale contacts using two different SThM probes (KNT probe from Kelvin nanotechnology and doped Si probe). The authors reported that the thermal conductance of water meniscus consists of 6% and 4% of thermal contact conductance of these probe–sample interaction, respectively. Gomès' group made a comprehensive experimental study of the influence of water meniscus and proposed the relation between capillary forces and probe temperature. The authors concluded that the contribution of water meniscus is just 1% to 3% of solid–solid conductance and various factors might affect the heat transfer through water meniscus depending on the roughness of surfaces,[104] relative humidity,[104] hydrophobic and hydrophilic surfaces.[105]

3.3. Conduction Heat Transfer

3.3.1. Tip–Sample Exchange (Contact) Resistance

If the probe works in contact mode, the solid–solid conduction between probe tip and sample plays a great role. Shi et al.[1b]

© 2019 The Authors. Published by WILEY-VCH Verlag GmbH & Co. KGaA, Weinheim

Table 2. Effective heat transfer coefficient h_{eff}.

	h_{eff} [W m^{-2} K^{-1}] and G_{air} [μW K^{-1}]	Instrumentation
Thermocouple probes		
Thiery et al.[79]	h_{eff} = 2300–13 000	2ω method: active thermocouple probe far away from samples
Wollaston wire probes		
David et al.[57]	h_{eff} = 1000 G_{air} = 4.25	Modeling of SThM measurement of thin films when probe far away from samples
Lefevre et al.[47b,52b]	G_{air} = 2.5[47b]	Modeling and experiment for Wollaston probe with DC current in vicinity of the sample
	h_{eff} = 800[52b]	Modeling and experiment for
Wollaston probe in air with DC current		
Zhang et al.[7a]	h_{eff} = 1900	Wollaston probe far away from samples
Wilson et al.[38g]	h_{eff} = 1722	Wollaston probe far away from samples
Chapuis et al.[98]	h_{eff} = 5000	Wollaston probe investigating pressure dependence of heat transfer coefficient far away from samples
Zhang et al.[19]	h_{eff} = 1700	Wollaston probe far away from samples
KNT/Pd probes		
Chui et al.[99]	h_{eff} = 3000	Experiment of two 8 μm wide low thermal conductivity sample
Spiece et al.[93]	G_{air} = 2	Experiment on SiO_2/Si heated sample for Pd resistive probe in air
DS probes		
Kim et al.[38d]	h_{eff} = 2000–7000	Modeling of Si cantilever and Si probe in air

proposed a 1D heat conduction model at the microscale for estimating the magnitude of solid–solid conduction and water meniscus conduction at the tip–sample contact assuming the heat transfer mechanisms are independent of each other. For measurements of micro/nanodevices with submicrometer probes, the contribution of air conduction reduces to a level smaller than that compared to the heat conduction at the tip–sample contact and across the water meniscus. Theoretical calculation of thermal exchange resistance proved to be an efficient way to understand the heat transfer mechanism of nanoscale constriction.[106] **Table 3** shows literature values for the thermal exchange resistance obtained from modeling and experiments. Typical results for the thermal exchange resistance are around 0.1–10 K μW^{-1}.

Figure 17 shows the temperature and cantilever deflection of a thermocouple probe in active mode. The experiment is performed under ambient conditions and shows that the temperature reading depends on the vertical position of the probe. The cantilever deflection is represented by the upper plots and the corresponding probe temperatures are in the lower ones. The heat conduction across the tip–sample contact begins with the liquid meniscus and increases with the contact force. The liquid film thermal conductance was at most equal to 3% of solid–solid thermal conductance. Thus, it is obvious that significant heat goes through the solid–solid conduction instead of the liquid.

3.3.2. Interfacial Thermal Resistance

When heat goes through the solid–solid contact between two samples, the reflection of the heat carriers that occurs at the interface results in a thermal boundary resistance.[74a,106a,111] The thermal boundary resistance between mechanical contact interfaces can be calculated using the following equation

$$R_{\text{contact b}}^{\text{th}} = \frac{R_{\text{b}}^{\text{th}}}{\pi b_{\text{c}}^2} \tag{6}$$

where R_b^{th} is a thermal boundary resistance with the unit m^2 K W^{-1} and b_c is the mechanical contact radius. The value of R_b^{th} value determined by experiments many times lie in the range of ≈5 × 10^{-9}–5 × 10^{-7} m^2 K W^{-1}.[38j,111a]

The tip–sample solid–solid contact however is never ideal due to surface roughness, contact pressure, and mechanical properties of contacting materials. A realistic model of the solid–solid contact interface contains multiple asperities that are schematically represented in Figure 16, and the smaller contact points between asperities bridge up the actual heat transfer paths.[47b] In ambient condition, the noncontacted regions are filled with liquid in air due to capillary condensation. Then the interfacial thermal resistance and the multichannel heat transfer through solid–solid contact can be regarded as nearly independent of contact quality when surface roughness of sample is less than several nanometers.[112] The heat transfer through multiple asperities and gaps needs to be analyzed separately depending on the these conditions: i) UHV, ii) extremely dry condition, iii) large surface roughness, or iv) when temperature at tip–sample contact is close to or greater than boiling point of water, as the filling effect of water meniscus is reduced. When the asperities are distant away from each other, the procedure of macroscale half-space heat source solution can be used to obtain interfacial thermal resistance.[113] Persson et al.[114] introduced a phonon heat transfer model to give R_b^{th} when the roughness of solid–solid contact interface is small enough to be assumed as flat interface condition and when temperature at contact interface

 © 2019 The Authors. Published by WILEY-VCH Verlag GmbH & Co. KGaA, Weinheim

Table 3. Theoretical calculations and experimental values of the thermal exchange resistance between probe tip and sample.

	R_c^{th} [K µW^{-1}]	Instrumentation
Thermocouple probes		
Luo et al.[33e]	9.5	Thermocouple-based SThM
Shi et al.[1b]	34.5 ± 7.1 (solid–solid contact) 149.3 ± 33.4 (liquid–solid contact)	Thermocouple-based SThM
Fletcher et al.[107]	100	Pt-Au nano-thermocouple-based probe contacts
Hwang et al.[9c]	4.4	Thermocouple based null-point SThM with suspended graphene
Shi et al.[1b]	10	Molecular dynamic modeling on silicon through 10 nm diameter orifice
Thermoresistive probes		
Park et al.[108]	25	Doped Si-based probes(silicon tip heated cantilever)
Nelson et al.[38j]	10	Doped Si-based probes contacts
Nelson et al.[106b]	10	Modeling with nanoscale thermal analysis
Lefevre et al.[47b,48b]	0.55 (tip radius of 5–15 µm) 0.17–0.21(heat transfer radius 100–300 nm)	Wollaston probe with probe tip radius of 5–15 [µm] The 5–15 µm refer to the tip curvature radii that are used to describe the torus geometry of the tip region.
Zhang et al.[7a]	0.11	Ballistic air conduction between Wollaston probe away from 50 to 200 [nm] samples
Zhang et al.[19]	0.13–0.26	Diffusive and transition air conduction between Wollaston probe away from 100 to 300 nm samples
Puyoo et al.[60]	4	KNT (Kelvin Nanotechnology) probe
Hinz et al.[65]	6	Microfabricated Si cantilevers with sharp heatable tip under vacuum with HfO_2/SiO_2 thin film
Gotsmann et al.[26]	50 (solid–solid contact) 833 (per atom–atom contact)	DS probe with tetrahedral amorphous carbon sample
Assy et al.[7b]	0.67	KNT probe
Menges et al.[9d]	2	DS probes with 80 nm diameter silicon nanowires under vacuum
Pumarol et al.[109]	SLG = 3.35/3.08 ± 0.03 BLG = 3.15 ± 0.03 BLG-trench = 2.75 ± 0.03 3LG = 2.98 ± 0.03 5LG = 2.76 ± 0.03 17LG = 2.58 ± 0.03	KNT probe on single layer graphene (SLG) bilayer graphene (BLG) and BLG suspended over the trench, following abbreviations are number of graphene layer
Ge et al.[97]	0.83	KNT probe on sub-100 nm gold wires
Others		
Prasher et al.[106a]	3.3–5	Modeling ballistic phonon transport between Si nanowire (Diameter = 20 [nm]) and Si substrate

is high. If the radius of these heat exchange contact points is smaller than the phonon MFP of either probe or sample, non-classical heat transfer effects must be considered instead of the classic diffusive regime.[11] Maassen et al.[115] claimed that Fourier's Law was still applicable in the ballistic regime by adapting the McKelvey–Shockley flux method[116] for heat transfer and phonon transport. The authors later proposed models that capture both diffusive and ballistic heat transfer based on Boltzmann transport equation. However, a more accurate approach was described by Gotsmann and Lantz, who analyzed the contact force dependence of quantized thermal contact conductance. The authors concluded that when the diameter of the heat exchange area is smaller than the transversal thermal coherence length (wavelength of thermal energy carrier in transversal direction),[117] the total thermal conductance at the interface can be expressed as the sum of each atomic contact conductance (G_{atom})[26]

$$G_{atom} = N\tau k_B^2 \pi^2 T_{int,m} / 3h_p \tag{7}$$

where k_B is the Boltzmann constant, h_p is Planck's constant, and $T_{int,m}$ is average interface temperature. The number of quantized modes N and transmission coefficient τ are obtained from mismatch models seen in refs. [74a,118]. The developed quantization model not only more accurately depicted quantum scale solid–solid contact thermal conductance but also enabled prediction of the number of contact points caused by multi-asperities when load force and R_{ss}^{th} were known. Experiments to validate this theory were carried out with specific tips in doped silicon probes operating in UHV-SThM.[26] However, this thermal contact conductance quantization model was then applied and confirmed to only work with the nominal contact pressure ≈500 MPa to ensure the contact condition according to the as developed model.

Other related investigations have explored the phonon heat transport through a nanoscale single-asperity contact between the probe tip and sample.[119] The nanoconstriction models determined the contact parameters, especially R_c^{th} taking the thermal boundary resistance R_b^{th} into account for better

© 2019 The Authors. Published by WILEY-VCH Verlag GmbH & Co. KGaA, Weinheim

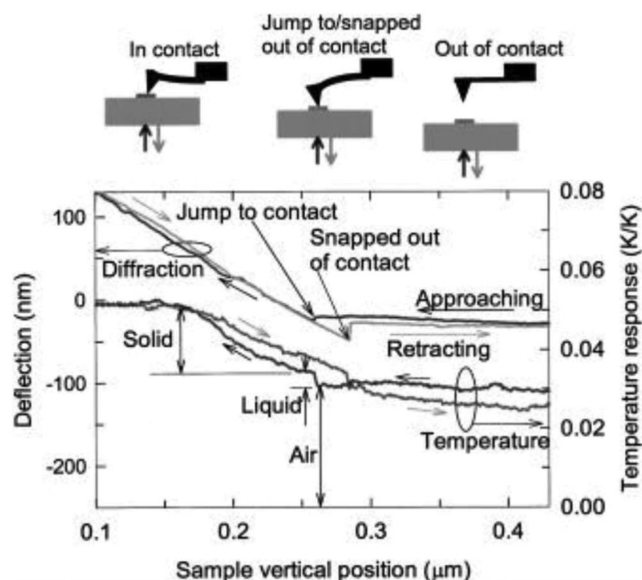

Figure 17. Cantilever position and the thermocouple-based probe temperature versus probe tip vertical distance over the sample surface. Reproduced with permission.[110] Copyright 2004, Springer Nature.

investigation of probe tip–sample interaction. Finally, it is worth noting that the authors suggested that the model and expression of the quantum thermal resistance might not be accurate when measuring above room temperature.[47b]

3.3.3. Probe Thermal Resistance

The thermal resistance of the probe, R_p^{th}, and the cantilever, R_{cant}^{th}, are necessary to obtain the sample properties and highly depend on the probe parameters, including geometry, shape and material, as well as the environment. We take DS probes, KNT probes and Pt probes as examples. For DS probes, which have high aspect ratio and the heater is somewhat away from the end of the tip, they can be assumed to have uniform temperature along the probe tip length without temperature variation inside the tip. Thus, R_{cant}^{th} and R_p^{th} can be approximated to infer the thermal resistance of Si nanowires.[1i,120] For KNT probes, the 3ω method and thermal conduction equation have been used to determine R_p^{th}.[48b,60] However, in general R_p^{th} and R_{cant}^{th} are difficult to quantify. Alternatively, the FEA is another approach applied to obtain R_p^{th} for KNT probes in air,[1e,71] which lead to the results of 5.06×10^4 K W^{-1}. However, the authors did not describe the details of the FEA model. For the Pt probe, Assy et al.[121] carried out experiments in vacuum and R_p^{th} was estimated to be 5.2×10^5 K W^{-1}. The probe thermal resistance in active mode needs accurate Joule heating power values, which were calculated from probe's electrical resistance and applied current. However, the authors assumed that the Pt thermoresistor at the tip possesses two-thirds of the electrical resistance of the whole probe. The total resistance of these probes depends on the electrical resistance of the NiCr current limiters, which makes difficult to determine accurately the tip electrical resistance. Small variations in the electrical properties of the NiCr current limiters that result from the fabrication process might lead to a large deviation of the resistance ratio. Ge et al.[97] used probes without current limiters obtaining a more accurate determination of the Joule heating across the resistor tip.

3.4. Thermal Radiation

Radiative heat transfer for distances between objects greater than Wien's wavelength (about 10 µm at ambient temperature), namely far-field radiation is well developed. If SThM system is not in vacuum, the radiation heat transfer is often neglected[122] or included into the effective heat transfer coefficient.[18a] However, if the gap size is less than Wien's wavelength, the near-field radiative heat transfer (NFRHT) occurs, and its behavior is not describable by conventional Planck's law due to dominating evanescent waves.[123] Shen et al.[124] proposed that when the distance is larger than 1 µm, the near-field radiation can be neglected regardless of the sample materials involved, since the near-field heat transfer coefficient calculated tends to be zero, as shown in **Figure 18**a. Figure 18 also supports that NFRHT for small gaps is able to go beyond the blackbody limit established for far field.[123] However, Cui et al.[125] showed only

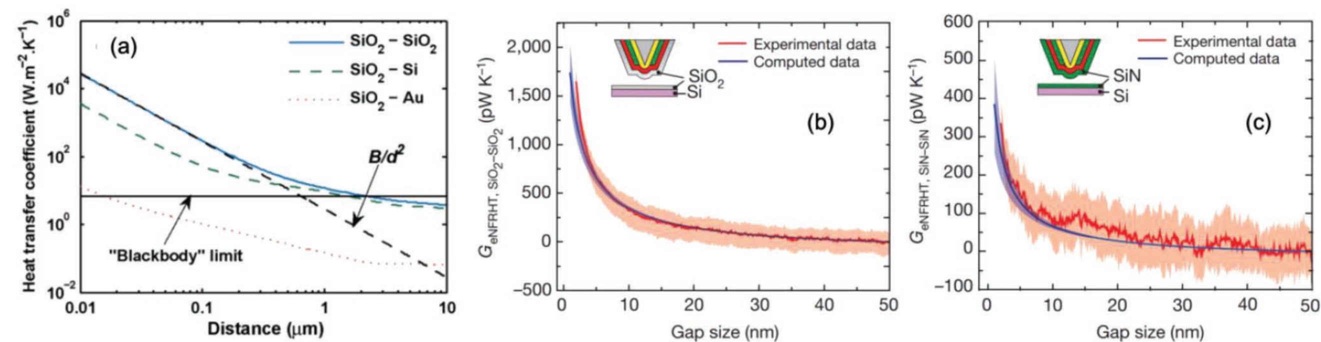

Figure 18. a) Calculated radiative h_{eff} as a function of the distance between two parallel plates. The black dashed line is the asymptotic line at small gaps between two glass plates. Reproduced with permission.[124] Copyright 2009, American Chemical Society. b,c) Measured thermal conductance due to NFRHT between SiO_2-coated probe (310 K) and a SiO_2 substrate at 425 K and between SiN-coated probe and a SiN substrate. The solid line is average conductance and the light color band is the corresponding standard deviation. The computational data are based on fluctuational electrodynamics. Reproduced with permission.[127a] Copyright 2015, Springer Nature.

© 2019 The Authors. Published by WILEY-VCH Verlag GmbH & Co. KGaA, Weinheim

limited NFRHT contribution to total thermal conductance of a single Au atom junction (due to dominance of conduction heat transfer), and validated Wiedemann–Franz Law's effectiveness down to the scale of single-atom contact. Investigations[12a,126] do concur that the radiative heat flux increases by orders of magnitude in near-field compared to the far-field. NFRHT is therefore imperative to be considered in vacuum conditions[12] and starts to affect the heat flow as soon as the distance between the two surfaces is smaller than the predominant wavelength.[3b] A numerical study by Nguyen et al.[12b] demonstrated that heat fluxes of NFRHT not only changed with the distance between two surfaces (δ) but also they depended on the radius of curvature of the tip (R). The authors defined the width of the half-maximum of heat flux distribution on the sample/substrate as the spatial resolution of NFRHT. A simple expression of this parameter was derived as it is proportional to $\sqrt{R\delta}$ when R was large and $\delta << R$. Recently, several experiments have been conducted to better understand nanoscale radiative heat transfer.[127] Kim et al.[127a] used homemade SThM thermocouple probes to measure NFRHT down to two nanometers gaps. The authors noted a sudden rise of thermal conductance in the extreme near field between metal and dielectric surfaces, as shown in Figure 18b,c indicating NFRHT increased dramatically when gap size got smaller than 10 nm. This experiment provided validation of a theoretical model developed based on fluctuational electrodynamics. Further investigation of extreme NFRHT for most materials and nanostructures were conducted by coating them onto the thermocouple probe.

In a different investigation Kittel's group pointed out that NFRHT measured between a probe tip coated with Au and an Au surface at distance of 0.2–7 nm was four orders of magnitude larger than what the theory of fluctuational electrodynamics predicted.[91b,92,128] Cui et al.[129] reported the measurement of near-field radiation for gap sizes between a thermocouple based probe and a heated Au sample from a few Å to 5 nm and operating in vacuum conditions. Based on this experiment, the authors indicate that the large discrepancy being observed between experiment and the predictions of fluctuating electrodynamics in some past reports[33h,130] might be due to surface contamination. This result will contribute to development of high-sensitivity measurements in the near-field radiative transport research.

In addition to fluctuational electrodynamics, there are other numerical methods used to simulate radiation heat transfer. The finite difference time domain method[131] mainly computes the heat transfer in arbitrary geometries with a statistical state. Thermal discrete dipole approximation[132] and the bulk field formulation of electro magnetism methods, which is an open-source and free software, implemented the frequency-domain volume-integral equation method of classical electromagnetic scattering[133] and include volume meshes modelling. The last numerical method is the surface-integral equation formulation of classical electromagnetism, which required less meshes compared to other numerical methods.[70]

Understanding heat transfer mechanisms is essential to develop better calibration strategies, which will be described in the next section. The comparison between the measurement results and modeling is key to understand the underlying physics. To this end, a series of techniques and methods have been established to make the measured results of thermal properties and temperatures of samples more accurate.

4. Calibration Techniques

The calibration in SThM is defined as establishing the relationship between what can be collected and measured, e.g., electrical signals or mechanical feedbacks, and parameters like temperature and thermal conductivity. In this section, we divide the calibration methods into five parts. In the first part (Section 4.1), thermal resistance models that describe the heat flow across probe–sample interaction for both in contact and noncontact modes are explained. The second part (Section 4.2) describes how temperature of a heated sample is calibrated. In the third part (Section 4.3), we discuss different samples and devices that can be used to calibrate the probe signal. In the fourth part (Section 4.4), we discuss the calibration process related with determination of the probe related parameters such as its dimension, geometry, and temperature. The last part (Section 4.5) elaborates different methods to calculate the sample and probe interaction, i.e., thermal exchange resistance (R_c^{th}) and heat transfer radius (b), also known as effective thermal exchange radius.

4.1. Heat Flow and Thermal Resistance Model

For all the SThM, the heat flow between the sample and tip is determined by the energy equation considering a sample, a thermal probe in contact or noncontact mode, and their interaction with ambient surrounding, as shown in Figure 16. The heat flow between the probe tip and the sample Q_{s-t} or Q_{t-s} depends on the probe, sample thermal properties, and temperatures plus surroundings.

In order to better understand the heat transfer mechanism between the probe and sample, a thermal resistance model was first developed by Luo et al.[33e] in 1990s. Through the investigation of the probes, samples, and measuring methods,[1b,9b,10c,47a,57] the heat transfer mechanisms become more clear and comprehensive. The heat flow diagram is shown in Figure 16a and can be separated into the two cases listed below.

4.1.1. Active-SThM with Thermocouple or Resistive Probe In-Contact/Noncontact Mode

The probe acts as a heat source if it is in active mode. Q_{Joule} is the total heat generation due to Joule heating of the probe or sometimes optical heating.[39d] The heat is dissipated through the sample, directly to the ambient and through the cantilever. The Q_{t-s} is the heat flow from the probe to the sample, which could be used to determine the thermal conductivity of the sample.[1e,18a,33e,56b,57,60,95,106b,122,134] In the active mode, Q_{t-s} can be expressed as

$$Q_{t\text{-}s} = \frac{T_{tip} - T_a}{R_s^{th} + R_c^{th}} \quad (8)$$

© 2019 The Authors. Published by WILEY-VCH Verlag GmbH & Co. KGaA, Weinheim

where R_c^{th}, R_s^{th}, T_a, and T_{tip} are thermal exchange resistance, sample thermal resistance, the ambient-room temperature, and probe tip temperature, respectively. For bulk and thick samples, the thermal resistance of the sample can be expressed as[18a]

$$R_s^{th} = \frac{1}{4k_s b} \tag{9}$$

For thin films and multilayer structures, the heat transfer across different layers and substrate must be considered. 1D heat conduction can be applied when the crossplane heat transfer across a film with thickness d that is sufficiently small and deposited on a semi-infinite substrate dominates. Then, the sample thermal resistance can be determined by the following equation[135]

$$R_s^{th} = \frac{d}{k_f \pi b^2} + \frac{1}{4k_s b} \tag{10}$$

where k_f and k_s represents the film and substrate thermal conductivities, respectively. The assumption of 1D crossplane heat transfer with a disc shape thermal exchange area is valid under certain circumstances. First, k_f needs to be much smaller than k_s to ensure that crossplane heat transfer dominates the overall heat transport inside the thin film. Second, the thermal exchange radius must be much larger than thin film thickness ($b >> d$) to guarantee a concentrated heat exchange area. The size of the probe affects the thermal exchange radius but as long as the above conditions are met, Equation (10) is valid. In order word, larger probes may be needed to measure thicker films on substrate.

Equation (8)–(10) can also be used in noncontact mode. One should note the temperature distribution along the resistive probe needs further thermal analysis to obtain the T_{tip}. Some other thermal resistances that should be considered include the path from the probe directly to the ambient, e.g., by using an effective heat transfer coefficient h_{eff} related with the heat loss from probe to the ambient. The heat flow through gap Q_{gap} between the cantilever and sample is typically insignificant compared to other heat losses and is neglected for both active and passive modes.[10c]

4.1.2. Passive-SThM with Thermocouple or Resistive Probe In-Contact/Noncontact Mode

According to heat flow diagram in Figure 16a, heat $Q_{s\text{-}t}$ flows from the sample to the probe and is directly dissipated to surroundings $Q_{p\text{-}a}$ and through the cantilever Q_{cant} which yields

$$Q_{s\text{-}t} = Q_{p\text{-}a} + Q_{cant} = \frac{T_s - T_{tip}}{R_c^{th}} \tag{11}$$

where it can also be expressed in terms of R_c^{th}, T_s, and T_{tip}. T_s is the sample temperature. The detailed thermal resistance network is well documented in ref. [10c]. If a thermoresistive probe operates in the passive mode, similar to what has been done with thermocouple-based probes in refs. [39f,79] T_{tip} can be determined through an energy balance to develop the expression of the heat transfer between the probe tip and sample.[136]

The difference between actual sample temperature and measured probe tip temperature needs to be determined through two ways: i) a calibration process that determines thermal exchange parameters, i.e., R_c^{th} and b, that allows to quantify $Q_{s\text{-}t}$[137] and ii) and a process that consists on nullifying $Q_{s\text{-}t}$.[64,134c,138] When taking R_c^{th} into account, the heat transfer between the probe tip and the sample is always assumed to be through a disc-like area with radius of b. Figure 16b decomposed R_c^{th} according to Equation (3), where air conduction is further divided into diffusive and ballistic regime.[33h] The noncontact mode difference is eliminating R_{ss}^{th} terms and R_w^{th}, while operation in high vacuum environment removes R_w^{th} and R_{air}^{th}.[37]

4.2. Calibration Samples

The self-heating calibration tests consists of using tiny metallic resistors on a membrane[139] or metallic lines that are heated by Joule effect[17a,18b,38e,69,85,130b,135,136,140] and that can be measured simultaneously with the SThM probes. The sample temperatures are independently measured through Johnson–Nyquist noise,[141] or using the TCR of the metal resistor lines, especially for Pt and Pd resistor lines due to their high TCR.

4.3. Probes Calibration

4.3.1. Passive Samples to Calibrate the Active Probes

The calibration is carried out using several bulk samples of known thermal conductivities from 0.1 to 100 W m^{-1} K^{-1} that correlate the signal of the probe with different thermal conductivities, as can be seen in **Figure 19**. The average probe temperature T_m is kept constant during the scanning, with varied currents, thus for each known conductivity sample, the relation between the change in probe power dissipation and the sample thermal conductivity is established.[142] Several researchers used similar methods to obtain the unknown thermal conductivity of samples from fitting their measurements with a calibrated curve similar to those presented in Figure 19.[1g,142–143] Figure 19 shows that the thermal conductivity of reference samples measured by SThM experiments can be fitted as a function of the SThM signal using an analytical model.[1g,94,143b]

Another calibration method for active mode SThM used reference samples with well-defined melting temperatures.[3a,38j,44d,144] The onset melting temperature measured by differential scanning calorimetry was regarded as the reference temperature used for the calibration process. However, the calibration techniques for SThM measuring polymeric materials' melting temperature still needs to be improved, since accurate calibration is hard to be achieved especially for commercially DS probes by this method.[94]

4.3.2. Active Samples to Calibrate the Passive Probes

Since 1990s, calibration of thermovoltage-based probes first used a macroscopic stage with a Peltier module.[33e] In later

© 2019 The Authors. Published by WILEY-VCH Verlag GmbH & Co. KGaA, Weinheim

years, hot-plate stages[32,33h,38p,49] were used to calibrate SThM signals. However, the probe tip size of SThM is smaller than the sample's active area, leading to calibration inaccuracies. To avoid heating the whole area, metal lines of variable widths were used for calibration purpose.[145] Another calibration method is Raman spectroscopy to determine a reference temperature,[146] but its large sensing area compared to the SThM tip leads also to inaccuracy. A different method employs a microfabricated stage with Johnson noise ref. [140a] and requires an integrated thermovoltage-based sensor on the microstage.

4.4. Probe Parameters Calibration

The SThM probes available on the market have various tip sizes or shapes. The most precise method to determine the thermoresistive probe parameters is achieved by a frequency sweep based on the 3ω method to measure the amplitude and phase of the thermal signal during Joule heating of the probe with an AC current with angular frequency 1ω.[18a] The experimental magnitude and phase plot of the 3ω signal of the probe versus frequency, obtained in air, was fitted with heat transfer modeling equations using probe parameters as variables. From this fiting, one can determine for example the conductive filament length and diameter of a Wollaston probe.[52b] 3ω calibration was not only able to provide modelling parameters for Wollaston probes but for other thermoresisitive probes, like Pd probes.[147] Puyoo et al.[147] analyzed the Pd probe and showed the cutoff frequency was increased as the dimension of the probe becomes smaller. Therefore smaller probes are better for higher temporal resolution. Other thermoresistive probes could also utilize this calibration strategy to obtain high precision probe dimensions.[148] In all, the probe parameters, such as the tip sizes, shapes, resistivities, and effective heat transfer coefficient, can be calibrated by the analytical model.[60]

For resistive-based probes, the accuracy of the probe temperature measurement can be improved by modifying the Wheatstone bridge,[38l,49] as explained in Section 2.6.1, and utilizing the 3ω method[52b] for the probes. For the DS probe, the nonlinearity between its electrical resistance and temperature makes its temperature calibration more complicated.[120]

For thermovoltage-based probes, its temperature can be derived from the thermoelectric voltage. However, since the thin film embedded in thermocouple junctions have lower thermopower than bulk ones, the calibration of the probe temperature should be carried out before the measurement starts.[1b]

4.5. Thermal Exchange Parameters Calibration between Tip and Sample

There are two parameters that are crucial to understand the heat transfer mechanism between the probe and sample, R_c^{th} and b. In this section, we will discuss how different approaches determine these parameters in two categories of SThM measurements, i.e., temperature sensing and thermal property characterization on sample.

4.5.1. Temperature Sensing Calibration

Due to the temperature difference between the probe tip and the sample surface resulting from the thermal exchange resistance, several calibration methods have been proposed.

The first method is monitoring heat flow between probe and sample, such as from picowatt heat flow calorimeter[137] or NP-SThM[64,134c,138] in order to reach zero $Q_{s\text{-}t}$. The NP-SThM first developed by Chung et al.[64,134c,138] used two scans with and without contacting the sample.[138] By applying a range of power to the probe, the sample temperature can be deduced by interpolating the probe temperature where the $Q_{s\text{-}t}$ is equal to zero. Then the sample temperature will be the same with the probe temperature in contact mode. The double-scan technique[39f,134c] is used to obtain thermal contact signals by scanning twice the sample in both contact and noncontact modes with the 100 nm clearance between tip and sample. The difference between the two thermal signals is due to the heat transfer through the tip–sample and is used to extract the sample temperature. The data reduction procedure is using the shared thermal equation with different boundary conditions (contact and noncontact), where the subtraction between them eliminates the air conduction term in common. However, the results obtained with this technique are rarely repeatable.[97]

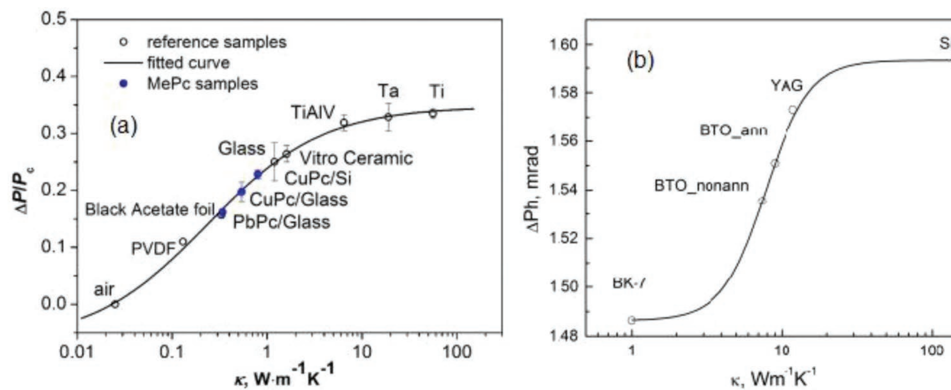

Figure 19. The SThM experimental signals versus thermal conductivity of different samples. a). MePc samples with reference samples. Reproduced with permission.[143b] Copyright 2013, Elsevier. b) References samples versus relative SThM phase signal. Reproduced with permission.[1g] Copyright 2013, Elsevier.

© 2019 The Authors. Published by WILEY-VCH Verlag GmbH & Co. KGaA, Weinheim

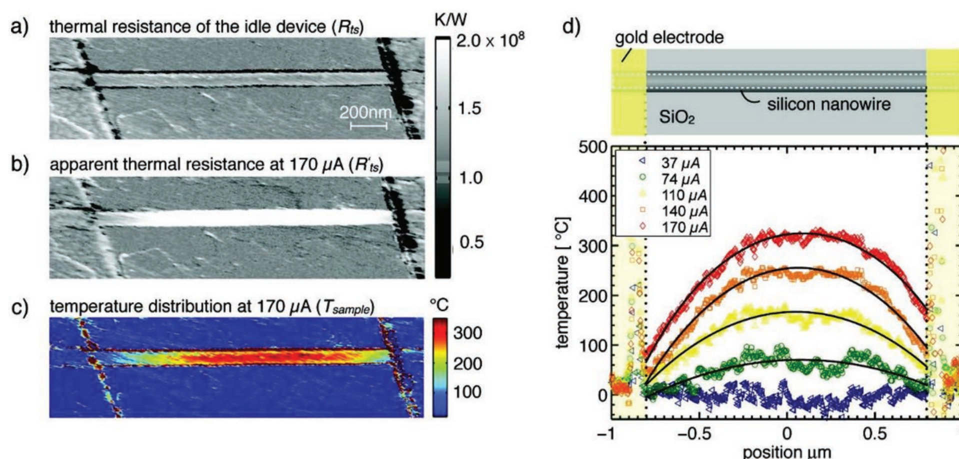

Figure 20. Temperature and thermal resistance profiles of 80 nm diameter Si nanowire (NW) at different heating powers, where 2D image showing distribution of highest temperature elevation was shown. a) Thermal exchange resistance of nonheated nanowire. b) Thermal exchange resistance of heated nanowire. c) Temperature distribution of nanowire surface obtained from (a) and (b). d) Temperature profiles of the heated nanowire with the different input current. Reproduced with permission.[9d] Copyright 2012, American Chemical Society.

Menges et al.[9d] developed two-scan methods to obtain the temperature distribution of a silicon nanowire connected between two electrodes by determining the change of the probe thermal resistance between contact and noncontact modes with the sample heating-on and off, respectively. Assuming the thermal exchange resistance remains the same in both cases, the variation of thermal exchange resistance (R_c^{th}) was brought out by the additional heat transfer flow between the tip and sample caused by the temperature profile of the device. Thus, the true temperature of sample or heater can be derived from

$$T_s - T_0 = (T_m - T_0)\left(1 - \frac{R_c^{th}}{R_c^{th'}}\right) \quad (12)$$

where R_c^{th} and $R_c^{th'}$ are the thermal exchange resistance when the device is off and on, respectively. **Figure 20** shows the measured thermal resistance and temperature profiles with different heating currents for a silicon nanowire. Knowing the temperature profile and using the heat transfer model allows the calculation of the nanowire thermal conductivity (≈25 W m^{-1} K^{-1}) and nanowire-substrate interface thermal conductance per unit length (≈0.03–0.3 W m^{-1} K^{-1}).

Zhang et al.[19] proposed a novel tip–sample thermal exchange resistance correlation using numerical modeling for tip–sample clearances both in the diffusive regime and the transition regime to help calibrate temperature sensing by the ambient noncontact SThM. The resulting temperature measurements by the proposed calibration methods matched well the modeling results and TCR calculated sample temperature.

Recently, new calibration devices have been used to quantify the heat transfer between the tip and sample. New devices not only offer more controllable and uniform temperature distributions[136] but also act as a flux meter with rather high responsivity.[149] A good example is from Ge et al.,[150] where a Si nanomembrane thermal detector was measured by a passive Pt probe to determine the thermal exchange resistance, R_c^{th} is 8.33×10^5 K W^{-1}, with the help of a heat transfer model.

4.5.2. Thermal Properties Measurement Calibration

Likewise, probe parameters can be determined by fitting experimental data with models, some other parameters like R_c^{th} and b can also be obtained from analytical modeling. Lefevre et al.[151] used fin heat transfer model in DC regime to deduce a simple correlation relating the thermal conductivity and probe currents or voltages and calibrate heat transfer parameters through the experimentally measured samples curves of 16 known samples. The authors concluded that experimental methods are more suitable to calibrate low thermal conductivity samples. However, R_c^{th} and b obtained by this method are the mean values based on the experimental data, which may lead to the inaccurate results. By solving similar energy equation in the AC regime, R_c^{th} and b can be obtained by measuring a set of samples with known thermal conductivity by using the 3ω method. It was concluded that the range of thermal conductivity reference samples should preferably cover the tested sample.[52b] One can also fit the experimental magnitude and phase of probe signals obtained from a frequency sweep. Thermal exchange parameters are determined by substituting probe parameters back to analytical expression.[52b,60,134b] In addition, Juszczyk et al.[71] and Puyoo et al.[38f] calibrated a thermoresistive Pd probe using modeling to fit the experimental probe data in air and under vacuum environment. Similarly, Ge and co-workers[136] fitted modeling temperatures of thermoresistor probes made of Si with experiments to quantify tip–sample interaction through air. Some researchers used various samples to obtain R_c^{th}. As an example, Assy et al.[121] utilized two different probes (KNT and Wollaston probe) on two samples (Silicon and Ge) to calculate the R_c^{th} by nanoconstriction model. Zhang et al.[7a] developed intersection methods to obtain b by performing measurements of two bulk calibration samples under the assumption of invariant R_c^{th} and b for low thermal conductivity samples. Later on, Wilson et al.[62] extended this method to various samples in the thermal conductivity range from 0.3–1.1 W m^{-1} K^{-1}. Other methods are also used to obtain thermal exchange parameters.

 © 2019 The Authors. Published by WILEY-VCH Verlag GmbH & Co. KGaA, Weinheim

For example, Puyoo et al.[38f] developed a calibration method using the Pd probe to determine R_c^{th} and b based on a step-conductivity sample. In this method, the probe scans across two neighboring areas of a patterned sample with different step heights and thermal conductivities. Then, b can be determined from the thermal signal profile occurring at the edge of the step between these two materials. In all, the assumption made by the above methods[7a,38f,52b,60,62,71,121,134b,136,151] is a constant R_c^{th}. However, R_c^{th} proved later to vary with the sample surface (the sample mechanical properties and roughness)[65,112b,152] and thermal conductivity.[65,111a,153] Wilson et al.[153a] provided an analytical expression for R_c^{th} as a function of various sample thermal conductivities.

Regarding calibration in vacuum environment, Hinz et al.[65] made an assumption that the thermal exchange resistance and $b = b_c$ does not change with the sample surfaces and used microfabricated thermistor tips in vacuum environment. In addition, the heat transfer between probe tip and sample was usually assumed to be 1D and thus the heat transfer area is modeled as a disk with the heat transfer radius b estimated by models from refs. [107,121]. To date, the probe tip–sample heat transfer radius b has equivalent size with the tip radius of curvature by experiments[38e,65,121,154] and the aforementioned calibration devices also helped in defining this parameter.

Considering different type of probes calibration, the above mentioned methodology[7,38f,62,71] can be applied to both Wollaston probe[7,62] and resistive Pd probe.[38f,71] However, the highly Si-doped probe has limited performance for these calibration methods due to nanoscale size effects. In fact, the MFP of crystalline Si, about 300 nm,[155] is larger than the tip apex sizes of the doped Si probes. It is much more complex for nanotip calibration, since the macroscopic description cannot fully describe the ballistic transport between probe and sample. To compensate the lack of an appropriate model, Gotsmann et al.[156] analyzed in detail the local heat transfer from heated tips and the sample surface. The authors proposed the Mathiessen rule to modify the MFP from the bulk material that take boundary scattering into account such that current microscale models could work. The authors also suggested an analytical expression for simple geometries.[156] Shi et al.[154] provided a heat transfer model in nanoscale suggesting that an extra thermal resistance should be added to better reflect the heat transfer at probe apex for a DS probe. Apart from the novel strategy discussed in Section 3.3.2, the relatively new Si doped probes need more attention on calibration.

In summary, calibration is the only and crucial step to capture the absolute tip–sample thermal exchange parameters as accurately as possible, especially when SThM deals with nanoscale phenomena. While current calibration methods certainly make temperature sensing of the sample more accurate, these methods still cannot determine the true temperature of the sample (sample temperature without the disturbance of the probes) as discussed in Section 2.3. As micro and nanodevices do not always operate in vicinity of probes to constantly monitor their thermal states, there may be discrepancy between sample operating temperature and measured sample temperature. This might be a crucial problem for measuring nano hotspot on devices, which could lead to malfunction of these devices, and more attention is needed towards determining the true sample temperature. In the following section, we discuss specific applications where thermal maps at the nanoscale are relevant.

5. Applications

In this section, we review the use of quantitative SThM measurements for the exploration of 2D materials, thermoelectric materials, phase change materials, polymers, biorelated materials, and other thermal phenomena as shown in **Figure 21**.

5.1. 2D Materials

The rapid development of 2D materials enables progress in a wide variety of fields, such as thermal management, optoelectronics, or highly integrated nanoscale electronic devices, among others.[38b,158] In this section, we present measurements of the thermal conductivity (Section 5.1.1) and temperature maps (Section 5.1.2) carried out by SThM in different types of 2D materials and devices including graphene, silicon, transitional metal dichalcogenides (TMDs) devices, and hexagonal boron nitride (h-BN) devices.

5.1.1. SThM Measuring Thermal Conductivity

Thermal measurements in graphene nanodevices require nanoscale spatial resolution and high sensitivity. Achieving such resolution is not always possible with techniques such as micro-Raman spectroscopy, with lateral resolution of ≈0.5–1 μm159 and a relatively low temperature sensitivity.[160] SThM is considered a successful technique to determine the thermal conductivity, k, of graphene with different sample geometries. For example, the in-plane k of a residue free suspended graphene bridge was measured by NP-SThM with spatial resolution reaching 50 nm.[39g] The authors measured the temperature profile of suspended graphene bridges and fitted the 1D heat transfer equation to obtain k of graphene bridges. Hwang et al.[9c] also used NP-SThM to obtain the in-plane thermal conductivity of suspended graphene disks whose radius ranged from 50 to 3680 nm. Their results also show that the increase of graphene size might make the ballistic resistance dominate the measured thermal resistance. Yu et al.[158c] obtained the temperature distributions of Joule self-heated graphene nanoribbons (GNRs) on silicon substrate by employing a thin film Pd resistive probe in dry Nitrogen environment with a spatial resolution less than 100 nm, as shown in **Figure 22**a. The probe was calibrated by Raman Spectroscopy, and using the 1D heat diffusion equation a thermal conductivity along the GNRs of up to 3800 W m^{-1} K^{-1} was estimated.

When graphene is stacked together, new thermal properties can be obtained. Pumarol et al.[109] directly obtained nanoscale thermal maps for single layer graphene (SLG) and few layer graphene (FLG) with about 50 nm lateral resolution using an UHV-SThM system. By a method similar to the two-scan method,[9d] the results show that an increasing number of layers can decrease the thermal conductivity of supported graphene. The measured in-plane thermal conductivities

© 2019 The Authors. Published by WILEY-VCH Verlag GmbH & Co. KGaA, Weinheim

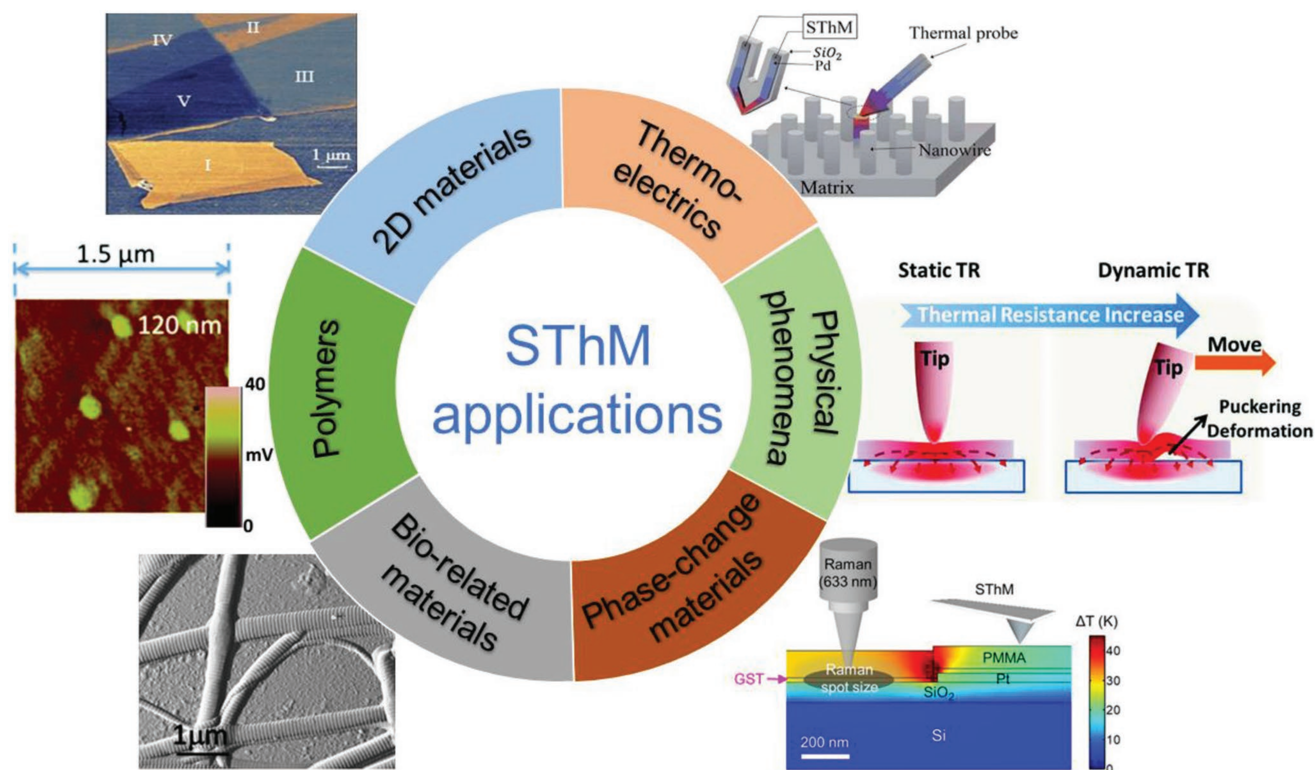

Figure 21. Overview of SThM applications with one example for each category. These applications will be elaborated in their corresponding sections in detail. Bio-related materials: Reproduced with permission.[8] Copyright 2011, Cell Press. 2D materials: Reproduced with permission.[38e] Copyright 2013, American Physical Society. Phase-change materials: Reproduced with permission.[146] Copyright 2017, Springer Nature. Polymers: Reproduced with permission.[157a] Copyright 2017, Springer Nature. Physical phenomena: Reproduced with permission.[157b] Copyright 2018, The Royal Society of Chemistry. Thermoelectrics: Reproduced with permission.[157c] Copyright 2016, The Royal Society of Chemistry.

were around 920, 317, 205, and 65 W m^{-1} K^{-1} for 1, 3, 5, and 17 layers of graphene, respectively.[27] Another study by Menges et al.[38e] showed a reduction of both in-plane and crossplane k with rising number of graphene layers supported on SiO_2 and SiC substrates by SThM with 6 nm lateral thermal resolution and sensitivity of each individual atomic layers, as shown in Figure 22b. This work served as validation of the analytical models of thickness dependence of graphene thermal properties. Tortello et al.[161] linked the in-plane and crossplane k of graphene to its defectiveness, as proved through a comparative study of reduced graphite oxide flakes prepared in both conventional and postannealing way. Samples were investigated using a Pd thin film thermoresistive probe in the active mode. The results show that an hour of 1700 °C postannealing effectively reduces defects in reduced graphite oxidizes nanoplates and enhances their thermal conductivity. This group further explored thinner single flake of multilayer graphene (MLG) and FLG properties supported on silicon or silicon oxide substrates. They demonstrated similar effects due to post annealing on these samples with a spatial resolution of ≈20 nm.[162] A summary table of graphene k for different conditions measured by SThM is given in ref. [27].

Gomès et al.[163] used SThM to study how the thermal conductivity of a mesoporous silicon thin film depended on the thickness and porosity. This film was used as an insulating element in integrated electronics. The results showed that the measured crossplane k of mesoporous silicon thin film was lower with increasing porosity, and it was strongly correlated to the film's nanometric thickness due to interfacial resistance effect. Another interesting effect in suspended 2D silicon materials was that the presence of native oxides change their thermal conductivity and thermal resistance in both in-plane and crossplane direction.[164]

5.1.2. SThM Measuring Temperature

Temperature sensing allows the determination of the heating profile in 2D related devices and it is commonly an intermediate step to determine the thermal conductivity of 2D materials, as shown in some of the examples given in Section 5.1.1.[39g,158c]

Choi et al.[165] used double scan technique to profile the temperature distribution around a local hot spot in graphene electronic devices deposited on oxidized Si and h-BN substrates and measured the thermal interfacial conductance and in-plane k of MLG. The results show that incrementing the thermal interfacial conductance and k can effectively decrease the hot spot temperature of devices made with a sub-10 nm gate dielectric supported by a high-thermal conductivity substrate. Unlike those reports for SLG devices fabricated on a Si substrate, NP-SThM measurements show that the temperature rise in flexible graphene devices is ten times larger.[112a]

© 2019 The Authors. Published by WILEY-VCH Verlag GmbH & Co. KGaA, Weinheim

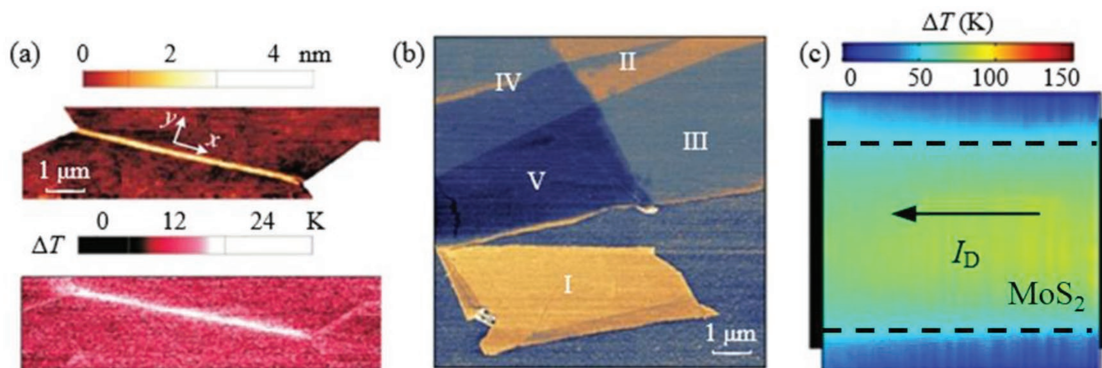

Figure 22. a) The top image is a topographic scan of a 3000 × 86 nm GNR and the bottom one is its corresponding SThM image for a Joule heating power of P = 78 µW. Reproduced with permission.[158c] Copyright 2011, American Institute of Physics. b) 2D Temperature distribution of different layers of graphene on SiO_2. Reproduced with permission.[38e] Copyright 2013, American Physical Society c) 2D uniform temperature distribution of MoS_2 transistor measured by SThM. Reproduced with permission.[158a] Copyright 2017, Nature Research.

Other than graphene, 2D materials such as transitional metal dichalcogenides (TMDs)[166] have been recently investigated in nanoelectronics. Determining how the energy dissipates in these devices is key to understand the limitations in their performance.[167] For example, Yalon et al.[158a] determined the thermal boundary resistance of MoS_2 on SiO_2/Si substrate by Raman spectroscopy and validated the uniformity of temperature distribution of MoS_2 by SThM, as shown in Figure 22c. Similarly, SThM confirmed the temperature uniformity on artificially stacked graphene, MoS_2 and WSe_2 thin film devices which were discovered to possess ultrahigh thermal isolation.[168] When studying MoS_2/WS_2 lateral heterojunctions and single layer MoS_2 grain boundaries using SThM, Yasaei et al.[169] observed nonuniform heating at MoS_2 grain boundaries that indicated nonuniform current flow across them. They asserted that dislocations at MoS_2 grain boundaries can largely explain a local increase in Joule heating, while MoS_2/WS_2 lateral heterojunctions did not induce localized heating.

In contrast, h-BN is a special class of hexagonal layered material with wide band gaps but high thermal conductivity.[158b] These properties make this 2D material ideal for electronic applications, where it could be used as a thin dielectric layer and to improve heat dissipation in devices. As an example, hot spots on a graphene device can be reduced at the maximal factor of 4.1 by coating it with another 2D layer of h-BN, which was demonstrated by double-scan based SThM.[170]

In conclusion, SThM was proved to be a successful tool for measuring k of graphene and other 2D materials. It presents nanoscale spatial resolution and high sensitivity under different sample configurations. As the configuration of nanoelectronic devices are becoming more complex and seeking greater functionality over a limited size, the future SThM studies should perhaps focus on revealing the possible anisotropy of thermal properties in 2D materials and the temperature distribution across grain boundaries of 2D heterostructures.

5.2. Thermoelectric Materials

Thermoelectric materials can convert thermal energy into electricity, and vice versa. They can be used in energy harvesting devices to take advantage of the residual heat generated by a system to improve the overall performance or efficiency. The parameter to evaluate and quantify thermoelectric effects is called the figure of merit ($zT = (\sigma \cdot S^2/k) \cdot T$), which is proportional to the electrical conductivity (σ) and the square of the Seebeck coefficient (S) and inversely proportional to the thermal conductivity (k) of the material.[18a] The ultimate goal for thermoelectric material synthesis is to increase the power factor, i.e., $\sigma \cdot S$,[2] and to decrease the thermal conductivity, a material classically known as electron-crystal phonon-glass. Nanostructured materials reported an increment in the thermoelectric performance compared with the bulk ones, since the increase of phonon scattering and quantum confinement can be observed in these structures.[157c] SThM serves as a useful method to characterize nanoscale thermoelectric materials as it has already been used to acquire qualitative thermal conductivity contrast images or quantitative thermal conductivity measurements with sub-100 nm resolution.[10c]

5.2.1. 3ω-SThM

3ω-SThM was applied to determine the thermal conductivity of several thermoelectric materials. As an example, the thermal diffusivity of Bi_2Te_3, a well-known thermoelectric material, was reported by Varandani et al.[171] using SThM combined with Parker's flash method. The thermal conductivity of ≈300 nm diameter Bi_2Te_3 nanowires, shown in **Figure 23**, and measured by 3ω-SThM method[38g,172] and high vacuum thermal scanning wave microscopy[173] was reported to be slightly lower than that of bulk. Further SThM measurements carried out by M. Muñoz Rojo et al.[172] showed that the thermal conductivity of Bi_2Te_3 nanowires reduced more than 70% (from 1.78 ± 0.46 W K^{-1} m^{-1} to 0.52 ± 0.35 W K^{-1} m^{-1}) when its diameter decreased from 300 to 25 nm.

Perez-Taborda et al.[174] reported $Si_{0.8}Ge_{0.2}$ nanomeshes with thermal conductivity down to 0.55 ± 0.10 W m^{-1} K^{-1} and n-type Ag_2Se film with 0.64 ± 0.10 W m^{-1} K^{-1}, being both obtained by 3ω-SThM at room temperature. Si and SiGe nanowires were discovered to have size effects on thermal conductivity at 50 nm and 480 nm diameters respectively, when measured by 3ω-SThM.[147b]

© 2019 The Authors. Published by WILEY-VCH Verlag GmbH & Co. KGaA, Weinheim

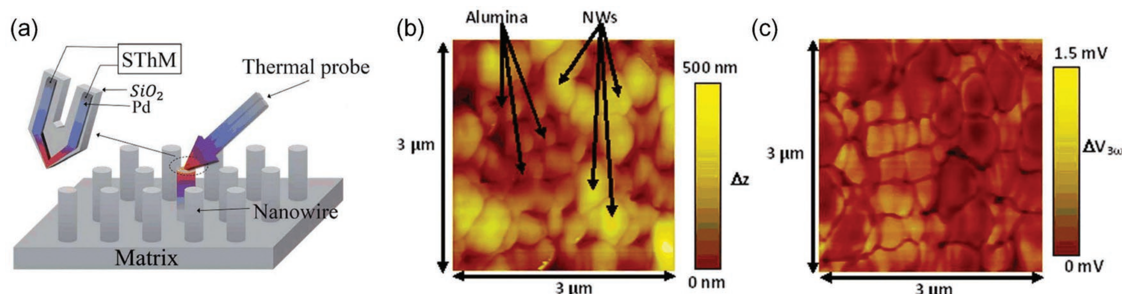

Figure 23. a) Schematic of nanowires *k* measurement by SThM method. Reproduced with permission.[157c] Copyright 2016, The Royal Society of Chemistry. b) SThM topographic image where yellow spots show the presence of nanowires. c) 3ω-SThM thermal map where the central dark region at the nanowires is due to the increase of heat flux. Reproduced with permission.[172] Copyright 2013, American Institute of Physics.

5.2.2. Other SThM Approaches to Measure Thermoelectric Materials

Several other SThM techniques for thermoelectric materials are documented. Recently Ghaderi et al.[175] successfully implemented thermal conductivity measurements of nanoparticles and nickel-nanowires built in silica aerogels by Passive-SThM accompanied with hot disk transient plane source method. The technique used a Peltier heating stage with passive mode probe and could measure Seebeck Coefficient as well. In molecular scale samples, Kim et al.[176] demonstrated by UHV-SThM measuring temperature distribution that electrostatic control can simultaneously increase electrical conductance and Seebeck coefficient of molecular junctions in vicinity of Au-biphenyl-4,4'-dithiol-Au and Au–fullerene–Au junctions. Kempf et al.[177] compared thermoelectric nanostructured half-Heusler alloys $Hf_{0.25}Zr_{0.75}NiSn_{0.99}Sb_{0.01}$ with great potential in waste heat applications. Before and after proton irratiation, the samples showed electrical and thermal conductivities to be reduced by 24% without changing the Seebeck coefficient. Similarly, SThM was used to carry out thermal conductivity maps in a both semiquantitative and in-depth way for the cross-section of a proton-irradiated ZrC sample, by fitting a curve of known thermal conductivity materials.[178]

As explained above, the combination of the 3ω method, which is a well-developed and quantitative method, with the SThM resulted in a successful technique for measuring the thermal conductivity of multiple thermoelectric materials. Yet enhancements could include subsurface scanning and higher spatial resolution.

5.3. Phase Change Materials

Nonvolatile memory devices, like PCM or RRAM, present excellent data retention, high read and write speeds, and low switching power.[28b] Additionally, RRAM have long-cycling endurance and good scalability. By reversibly switching chalcogenide materials between amorphous and crystalline states, the data storage of PCM produces considerable reflectivity changes to be employed by optical read devices, and electrical conductivity modulation for solid state devices.[28a] When the amorphous state, often referred as the high resistance state, switches to crystalline, i.e., the low resistance state, the devices undergoes a process called SET and the reverse one is called RESET.[28b,146] SThM can be used to measure the thermal properties of these states with high resolution.[2]

5.3.1. Active-SThM Measurement

Saci et al.[179] investigated the thermal conductivity of phase change material, crystalline Sb_2Te_3 nanowire (NW), along transverse direction by 3ω-SThM. The measured thermal conductivity value for the NW is 0.93 ± 0.1 W m^{-1} K^{-1} which is comparable to the reported bulk value. Bosse et al.[28a] used a commercial SThM in active mode to study the phase-change threshold and thermal conductivity of $Ge_2Sb_2Te_5$ (GST) thin film qualitatively and quantitatively. They determined that the thermal conductivity of GST in crystalline and amorphous state was 1.60 and 0.20 W m^{-1} K^{-1}, respectively. Battaglia et al.[180] measured the interfacial thermal boundary resistance between GST and SiN and the thermal resistance along the thickness of In_3SbTe_2 crystalline nanowires using 3ω-SThM. The thermal boundary resistance between the phase change materials and heating devices was a significat contributor to thermal resistance and therefore affects the heat required to reach the phase-change temperature.[181] GST nanowire led to lower programming currents, which required a lower power for amorphization.[181] In_3SbTe_2 nanowires having two times higher phase-change temperature than GST also exhibited by 3ω-SThM at least two times higher thermal resistance than the bulk material and thus could improve the scalability of PCM devices.[180] Additionally, in RRAM devices, Hinz et al.[65] determined the *k* of 3 nm HfO_2 to be 0.27 W m^{-1} K^{-1} during vacuum SThM in DC-active mode.

5.3.2. Passive-SThM Measurement

Yalon et al.[146] combined Raman thermometry and SThM operating in DC passive mode, to calibrate the surface temperature measurements of SThM in GST memory devices, as shown in **Figure 24**a.

High resolution SThM is able to map relative temperature profiles on electrical devices while Raman spectroscopy can determine the absolute temperature on materials that present Raman signature. The Raman temperature reading can be used to calibrate the actual SThM profiles. Fong et al.[182] applied the above technique on their dual-layer dielectric stack PCM composed of SiO_2/Al_2O_3 insulator and showed that a 60% reduction can be observed in the reset energy in comparison with SiO_2-isolated devices. Similarly,

© 2019 The Authors. Published by WILEY-VCH Verlag GmbH & Co. KGaA, Weinheim

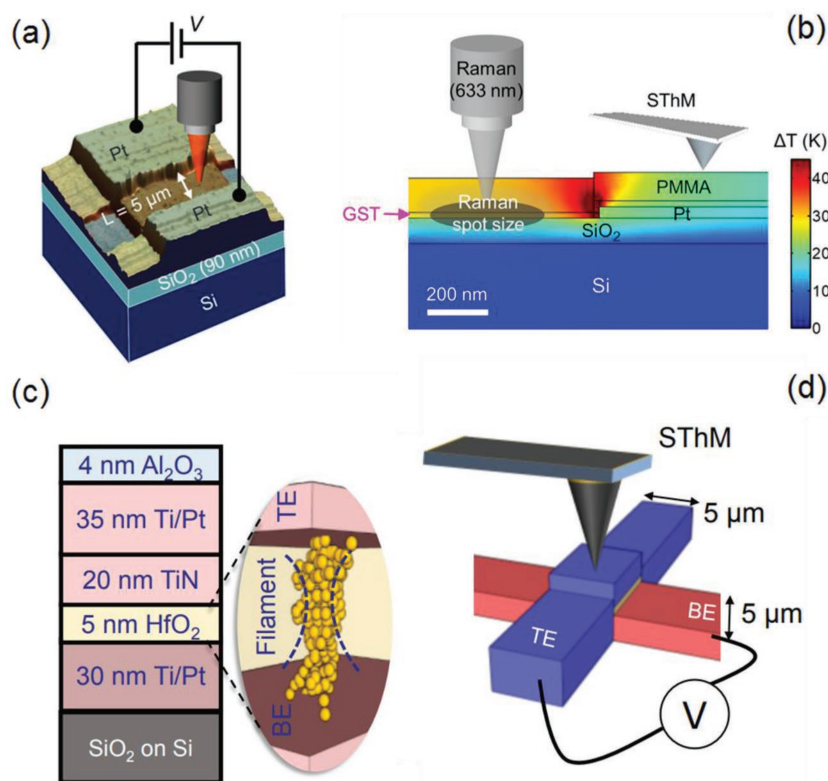

Figure 24. Thermometry of memory devices. a) Experimental setup: SThM operated with a GST heated sample. b) Finite element model of the temperature profile of the device near the electrical contact that is measured by Raman thermometry and SThM. c) Schematic drawing of a HfO_2 RRAM memory device. The inset shows the conductive filament formed in this device. d) SThM setup with an electrically biased device. c,d) Reproduced with permission.[145] Copyright 2018, IEEE.

Deshmukh et al.[145] measured the heating of conductive filaments in 5 nm HfO_2 RRAM devices by Passive-SThM, which was calibrated by self-heated metal lines. Datye et al.[183] used SThM and modeling to investigate the memory switching process of $MoTe_2$ devices.

As the memory devices scale down with the goal of optimizing their design and fabrication, the SThM can play a key role in investigating the thermal properties of the new materials and devices. However, when the hot spots or devices become smaller than the thermal exchange radius or when hot spots are located underneath the sample surface, the SThM data reduction would be challenged and more complex analysis of the probe signal should be carried out.[145]

5.4. Biorelated Materials

Alternative SThM methods for investigating the heat transport in biological medium are needed in biomedical and organic material related research. Nakanishi et al.[184] found the glass transition temperature and linear coefficient of expansion of bacterial vegetative cells and spores by monitoring cantilever deflection during phase transition of cells. Assuming that the thermal conductivity reduces with the increase of heat applied, this group proposed an SThM method that holds constant cantilever and probe temperatures at near transition temperature to measure k of biological cells and spores.[185] Haeberle et al.[186] demonstrated that a Joule-heated cantilever was able to scan simultaneously the thermal conductivity and topography with tip-size spatial resolution samples like proteoliposomes, hairs and collagen. The transition temperatures of collagen and gelatin in Figure 21 in hydrated and dry environments were measured by Bozec et al.[8] The µTA monitoring cantilever deflection versus Wollaston wire probe's temperature showed different degradation characteristics of collagen and gelatin. This investigation supports applicability of SThM in biophysics.

Investigation of thermal properties of wood cells at microscale had also been addressed by SThM.[187] For wood materials, SThM was introduced to analyze the penetration of resin in wood structure and to measure the size of the resin and wood substrate interface.[187,188] Xu et al.[187] imaged the thermal conductivity of red oak and rice straw cells, and later characterized thermal properties of oak fiber cell wall[189] and transition characteristics during carbonization of *Quercus rubra* wood fiber cell walls.[5] Their results proved the validity and potential of SThM in wood applications. Organic semiconductor CuPc layer was investigated by Active-SThM yielding to thermal conductivity in the range of 0.15-0.3 W m^{-1} K^{-1} that was determined from a calibration curve of known thermal conductivity materials.[143b]

The immerse SThM (i-SThM) technique[38r] can conduct measurement in liquid environments. However, currently other microscopies dominate live sciences studies. Thus, improved i-SThM methods or alternative SThM methods that can work in liquid surroundings could become in high demand.

5.5. Polymer Materials

In most of the cases, polymers present low bulk thermal conductivities and are usually considered as insulators. However, when orienting their polymer chains properly, polymers can present higher thermal conductivities than bulk and thus can be used as thermal interface materials in microelectronics.[3b] These samples can also benefit from SThM measurements.

As demonstrated by Boutaous et al.,[190] the melting temperature of bulk polymers depends on their microstructure distribution that is strongly correlated with processing history. By calibrating the probe tip temperature and cantilever deflection against curves of three known melting temperature samples, the authors determined that the higher crystalline structure leads to higher melting temperature. The thermal diffusivity of thin films of polyamide-imide could be scanned by flash method in TCM of SThM and their thermal conductivity in CCM of SThM.[191] Composites or laminates of polymers are

© 2019 The Authors. Published by WILEY-VCH Verlag GmbH & Co. KGaA, Weinheim

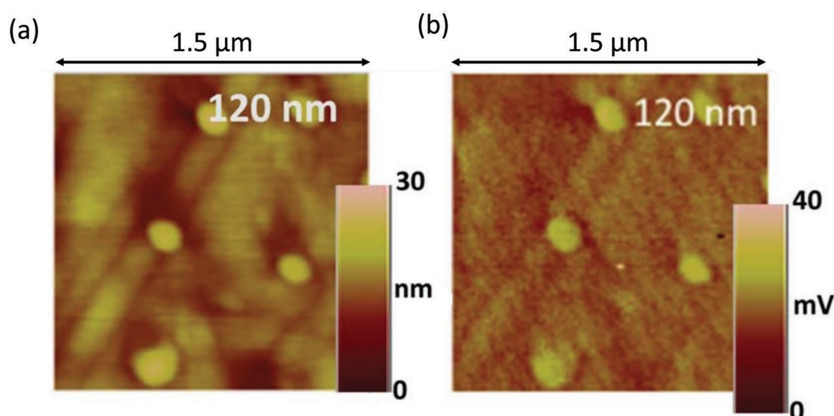

Figure 25. SThM a) topography and b) thermal image of 120 nm diameter P3HT nanowires. Reproduced with permission.[157a] Copyright 2014, Royal Society of Chemistry.

also of great interest. Hongo et al.[192] explored the interfacial thermal properties of polymers blends, specifically between linear low-density polyethylene (LLDPE)/isotactic polypropylene (*it*.PP) and LLDPE/deuterated polyethylene (D-PE), by SThM, X-ray diffraction and Raman spectroscopy. In TCM and contact mode, the SThM carried out thermal scans along the interfacial direction and the characterization of the size of interfacial region and adhesive strengths versus temperature were obtained and validated by other two techniques.

Another kind of polymers, like the Azobenzene-functionalized polymers, show nonlinear properties. By measuring the temperature rise of thin films in free-standing state, the azo-polymer thin film was concluded to have increasing photoinduced heating when it is laminated by a larger phonon intensity.[193] Researchers also combined thermally conductive fillers into polymers and built thermal percolation pathways to promote internal heat transfer in the composites. The interfacial analysis between poly(vinyl alcohol) and Fe_3O_4 filler by SThM in CCM showed the domination of the interfacial resistance in the thermal conduction and that the k of the composite increased when filler concentration was increased.[194] Reducing the dimensionality of the polymer can also contribute to modify the thermal properties of the sample. Muñoz Rojo et al.[157a] showed that the thermal conductivity of P3HT polymer nanowires measured by 3ω-SThM reduced as the individual diameter of the nanowires decreased and the polymer chain orientation changed. **Figure 25** shows a topographic and thermal image of 120 nm diameter P3HT nanowires measured during this study.

Another interesting polymeric thin film that was studied by dynamic SThM is worth mentioning here. Alq_3 thin film is pioneer in the field of organic electronics, forming organic light emitting diode with effective heterogeneous structure.[38b] Both the active and passive modes of SThM were used to measure temperature and the 2D thermal conductivity distribution in the thin film. Proving the feasibility of dynamic SThM, Heiderhoff et al.[38b] also suggested a model that was capable to monitor film thickness variation in all thin films, i.e., metallic, polymeric, and even insulating.

In summary, the SThM's ability for spatially confine heating and high spatial and temperature resolution allows to better understand polymer thermal and structural properties as well as the interaction between different types of polymers that are mixed together.

5.6. Characterization of Other Thermal Phenomena by SThM

Jeong et al.[195] quantified nanoscale Joule heating during electromigration of nanowires using UHV-SThM. Their results showed electromigration beginning at temperatures considerably lower than the gold melting temperature and voids predominantly accumulating at the cathode contributing to both local hot spots and asymmetric temperature profiles.

EC is the temperature change in electrically insulating materials caused by the alternating electric field, which could be applied for solid-state cooling. Kar-Narayan et al.[1f] demonstrated the capability of SThM to accurately capture the EC effect on a $BaTiO_3$-based multilayer capacitor (MLC), as shown in **Figure 26**.

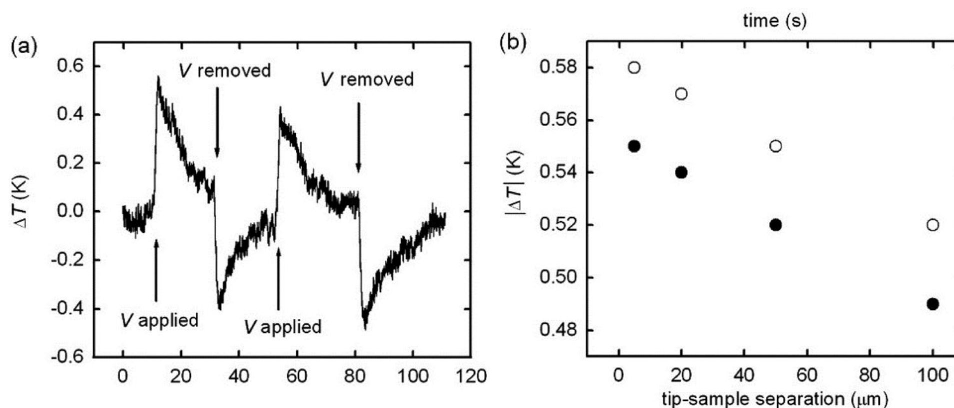

Figure 26. Effects in an MLC in SThM measurements. a) Temperature difference ΔT versus time, with applying and removing $V = 200$ V. b) EC heating (open circles) and cooling (closed circles) with the variation of tip–sample separation. Reproduced with permission.[1f] Copyright 2013, American Institute of Physics.

© 2019 The Authors. Published by WILEY-VCH Verlag GmbH & Co. KGaA, Weinheim

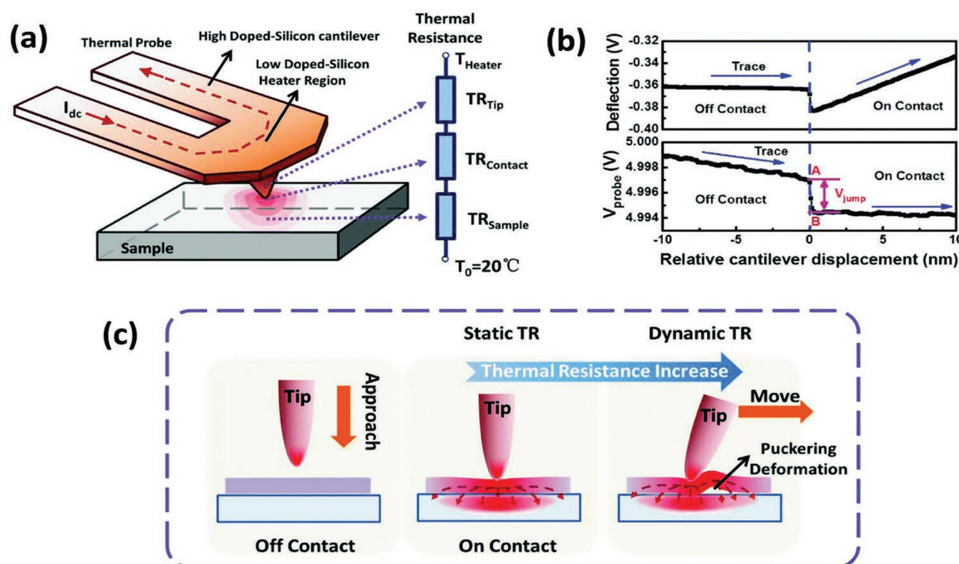

Figure 27. a) The schematics of SThM and puckering effect induced dynamic interfacial thermal resistance. b) The force/temperature approach-retreat curve of the MoS_2. c) The schematic diagram of origin of static and dynamic thermal resistances. Reproduced with permission.[157b] Copyright 2018, Royal Society of Chemistry.

The reversible EC effect and Joule heating was explored by SThM measurements on $0.9Pb(Mg_{1/3}Nb_{2/3})O_3$-$0.1PbTiO_3$ thin films. An experimental sequence method, similar to Figure 26, was used. In the first step, an electric field was applied to generate EC heat that heated up the probe tip and slowly dissipated the heat to the surroundings at a constant field. When the field was removed, cooling occurred and as time passed, the temperature restored to the ambient one. A maximum temperature difference of 4.2 K was reached in 13 µm thick film.[196]

The puckering effect is shown in **Figure 27**, and is a nanoscale local frictional characteristic usually occurring in the substrate–film–tip system, which is coupled with a dynamic interfacial thermal response at the same time. Xu et al.[157b] proposed a new mechanical–thermal coupling effect in monolayer/bilayer MoS_2 and WS_2 films that was observed by SThM, namely the enhancement of thermal boundary resistance induced by puckering deformation. It is shown that the puckering effect is dependent on the scanning velocity and the film thickness.

Anomalous Nernst effect (ANE) is an effect in which a generated electric field can be observed in mutually normal direction to both the magnetization and the thermal gradient within an electrically conducting material when the magnetization and thermal gradient are perpendicular to each other.[197] SThM could investigate the thermal gradient component of ANE that specified the Nernst coefficient of the measured material. To illustrate nanoscale ANE characterization, the CoFeB/Pt NWs of 300 nm width were perpendicularly magnetized. With a transverse directional temperature gradient, an ANE voltage would be induced along the length of the NWs. The temperatures of CoFeB/Pt NWs were measured by passive SThM with doped Si probe. The calibration was done by approximately a linear fitting between the probe electrical resistance and the temperature measured by a thermocouple on a SiO_2 substrate identical to the one under the sample. This was assumed valid for sample temperatures between 25 and 60 °C. Next, temperature gradient obtained by SThM was applied to output Nernst coefficient. The development of this SThM technique will be promising to improve the accuracy of the Nernst characterization measurements in the future.[84]

6. Conclusion

In this review we have covered the most recent developments of SThM and specifically emphasized the applications and enhancement of accuracy and resolution of this technique. We evaluated probe designs on critical parameters and performances and summarized new investigations of heat transfer mechanisms, especially on air conduction and near field radiation. We have also pointed out calibration strategies and their ranges of application, along with promising results from research fields where SThM, either commercial or homemade, is applied.

SThM applications concentrated on thermal conductivity and temperature characterization of 2D materials, thermoelectric materials, polymer materials, biorelated materials and phase change materials. Additionally, few other works focused on other thermal phenomena investigated by SThM such as electromigration, electrocaloric effects, anomalous Nernst effect and puckering effects.[157b] There are more potential areas where the high sensitivity and resolution of SThM can contribute to great progress. For example, the possibility of exploring nanoscale thermal properties of gene mutation process and profiling nanoscale electromigration[195] as a function of temperature in superconducting materials. SThM can also be integrated as a module onto well-established microscopy systems, by developing multifunctional probes that can measure sample's mechanical, thermal and even electrical properties in one setup.

© 2019 The Authors. Published by WILEY-VCH Verlag GmbH & Co. KGaA, Weinheim

Future challenges for SThM lie in both extending its applicability and in accurate consideration of the probe–sample heat transfer mechanisms. Regarding its applicability, the SThM has been shown to be a successful technique to gain thermal insights in different types of materials and devices. However, as the size of these samples shrink, further progress in this area is needed to achieve higher temperature reading accuracy, spatial resolution, temporal response and/or sensitivity. Moreover, the SThM was shown to be able to operate under different environments, e.g. under air, liquid, and rarefied gases.[38r] The immerse-mode SThM widens the current applicability of SThM to liquid environments, but attempts to employ this technique are limited. Further development would focus on designing specialized probes and calibration strategies for immerse environments.

Regarding heat transfer mechanisms, the most challenging is the contribution of near-field radiative thermal transport. Neglecting near field radiation has been validated experimentally for larger gaps and operation in air.[127a] Nevertheless, the understanding of near field radiation is imperative for quantifying its contribution in vacuum-operated SThM system,[37] as well as for characterization of the quantum scale behavior of electromagnetic waves in near field.[198] However the consideration of near-field radiation is largely in theoretical and numerical phase.[3b] Thus, experiments towards validating modeling results are necessary.

Conflict of Interest

The authors declare no conflict of interest.

Keywords

2D materials, calibration, heat transfer, micro and nanoscale thermal measurement, scanning thermal microscopy

Received: January 28, 2019
Revised: July 10, 2019
Published online:

[1] a) C. Dekker, *Phys. Today* **1999**, *52*, 22; b) L. Shi, A. Majumdar, *J. Heat Trans. ASME* **2002**, *124*, 329; c) B. Cretin, S. Gomès, N. Trannoy, P. Vairac, *Top. Appl. Phys.* **2007**, *107*, 181; d) C. Brites, P. Lima, N. Silva, A. Millán, V. Amaral, F. Palacio, L. Carlos, *Nanoscale* **2012**, *4*, 4799; e) P. Tovee, M. Pumarol, D. Zeze, K. Kjoller, O. Kolosov, *J. Appl. Phys.* **2012**, *112*, 168; f) S. Kar-Narayan, S. Crossley, X. Moya, V. Kovacova, J. Abergel, A. Bontempi, N. Baier, E. Defay, N. D. Mathur, *Appl. Phys. Lett.* **2013**, *102*, 032903; g) A. Kaźmierczak-Bałata, J. Bodzenta, M. Krzywiecki, J. Juszczyk, J. Szmidt, P. Firek, *Thin Solid Films* **2013**, *545*, 217; h) G. Wielgoszewski, M. Babij, R. F. Szeloch, T. Gotszalk, *Sens. Actuat. A: Phys.* **2014**, *214*, 1; i) S. Volz, G. Chen, *Appl. Phys. Lett.* **1999**, *75*, 2056; j) W. Lee, K. Kim, W. Jeong, L. Zotti, F. Pauly, J. Cuevas, P. Reddy, *Nature* **2013**, *498*, 209.
[2] A. Majumdar, *Ann. Rev. Mater. Sci.* **1999**, *29*, 505.
[3] a) J. Duvigneau, H. Schönherr, G. Vancso, *ACS Nano* **2010**, *4*, 6932; b) T. Luo, G. Chen, *Phys. Chem. Chem. Phys.* **2013**, *15*, 3389.
[4] E. Gmelin, R. Fischer, R. Stitzinger, *Thermochim. Acta* **1998**, *310*, 1.
[5] D. Xu, T. Ding, Y. Li, Y. Zhang, D. Zhou, S. Wang, *Wood Sci. Technol.* **2017**, *51*, 1.
[6] M. Kim, A. Giry, M. Mastiani, G. O. Rodrigues, A. Reis, P. Mandin, *Microelectron. Eng.* **2015**, *148*, 129.
[7] a) Y. Zhang, E. Castillo, R. Mehta, G. Ramanath, T. Borca-Tasciuc, *Rev. Sci. Instrum.* **2011**, *82*, 024902; b) A. Assy, Institut National des Sciences Appliquees de Lyon, Soutenue le **2015**.
[8] L. Bozec, M. Odlyha, *Biophys. J.* **2011**, *101*, 228.
[9] a) W. Jeong, S. Hur, E. Meyhofer, P. Reddy, *Nanoscale Microscale Thermophys. Eng.* **2015**, *19*, 279; b) S. Gomès, N. Trannoy, P. Grossel, *Meas. Sci. Technol.* **1999**, *10*, 805; c) G. Hwang, O. Kwon, *Nanoscale* **2016**, *8*, 5280; d) F. Menges, H. Riel, A. Stemmer, B. Gotsmann, *Nano Lett.* **2012**, *12*, 596.
[10] a) U. Wischnath, J. Welker, M. Munzel, A. Kittel, *Rev. Sci. Instrum.* **2008**, *79*, 073708; b) M. E. McConney, D. D. Kulkarni, H. Jiang, T. J. Bunning, V. V. Tsukruk, *Nano Lett.* **2012**, *12*, 1218; c) S. Gomès, A. Assy, P.-O. Chapuis, *Phys. Status Solidi A* **2015**, *212*, 477.
[11] R. S. Prasher, P. Phelan, *J. Appl. Phys.* **2006**, *100*, 063538.
[12] a) J. B. Xu, K. Lauger, R. Moller, K. Dransfeld, I. H. Wilson, *J. Appl. Phys.* **1994**, *76*, 7209; b) K. L. Nguyen, O. Merchiers, P. O. Chapuis, *J. Quant. Spectrosc. Ra. Transf.* **2017**, *202*, 154.
[13] J. Bodzenta, J. Juszczyk, M. Chirtoc, *Rev. Sci. Instrum.* **2013**, *84*, 093702.
[14] S. Kalinin, A. Gruverman, *Scanning Probe Microscopy of Functional Materials*, Springer, Berlin **2007**.
[15] M. Poggio, C. L. Degen, C. Rettner, H. Mamin, D. Rugar, *Appl. Phys. Lett.* **2007**, *90*, 263111.
[16] Y. Sugimoto, P. Pou, M. Abe, P. Jelinek, S. Morita, O. Custance, *Nature* **2007**, *446*, 64.
[17] a) M. Nikiforov, R. Proksch, *Scan. Probe Microsc. Func. Mater.* **2011**, 199; b) A. S. Chekanov, S. Alli, O. Kolosov, *IEEE Trans. Magn.* **1997**, *330*, 663; c) J. R. Withers, E. Aston, *Adv. Colloid Interface Sci.* **2006**, *120*, 57.
[18] a) T. Borca-Tasciuc, *Ann. Rev. Heat Trans.* **2013**, *16*, 211; b) F. Menges, H. Riel, A. Stemmer, B. Gotsmann, *Nature Commun.* **2016**, *7*, 10874.
[19] Y. Zhang, W. Zhu, L. Han, T. Borca-Tasciuc, *Rev. Sci. Instrum.* **2019** (Revised).
[20] a) L. Aigouy, L. Lalouat, M. Mortier, P. Löw, C. Bergaud, *Rev. Sci. Instrum.* **2011**, *82*, 036106; b) D. T. Peter, V. K. Oleg, *Nanotechnology* **2013**, *24*, 465706.
[21] Z. Chen, X. Shan, Y. Guan, S. Wang, J.-J. Zhu, N. Tao, *ACS Nano* **2015**, *9*, 11574.
[22] A. A. Kinkhabwala, M. Staffaroni, S. Ö, S. Burgos, B. Stipe, *IEEE Trans. Magn.* **2016**, *52*, 1.
[23] a) H. M. Pollock, A. Hammiche, *J. Phys. D: Appl. Phys.* **2001**, *34*, 7; b) D. Teyssieux, D. Briand, J. Charnay, N. F. d. Rooij, B. Cretin, *J. Micromech. Microeng.* **2008**, *28*, 9; c) D. Teyssieux, L. Thiery, B. Cretin, *Rev. Sci. Instrum.* **2007**, *78*, 225.
[24] G. Wielgoszewski, T. Gotszalk, *Adv. Imaging Electron Phys.* **2015**, *190*, 177.
[25] L. Shi, A. Majumdar, *Applied Scanning Probe Methods*, The Ohio State University, Columbus, OH **2013**.
[26] B. Gotsmann, M. Lantz, *Nature Mater.* **2012**,*12*, 59.
[27] K. Khanafer, K. Vafai, *Adv. Heat Transf.* **2016**, *48*, 95.
[28] a) J. L. Bosse, M. Timofeeva, P. D. Tovee, B. J. Robinson, B. D. Huey, O. V. Kolosov, *J. Appl. Phys.* **2014**, *116*, 134904; b) M. Lanza, *Materials* **2014**, *7*, 2155.
[29] C. Williams, K. Wickramasinghe, *IEEE 1986 Ultrasonics Symposium*, New York **1986**, 393.
[30] A. Majumdar, J. P. Carrejo, J. Lai, *Appl. Phys. Lett.* **1993**, *62*, 2501.
[31] R. Dinwiddie, R. J. Pylkki, P. E. West, *Therm. Conduct.* **1994**, *22*, 668.
[32] P. S. Dobson, J. M. R. Weaver, G. Mills, *Proc. IEEE Sens.*, Atlans **2007**, 708.
[33] a) A. Majumdar, J. Lai, M. Chandrachood, O. Nakabeppu, Y. Wu, Z. Shi, *Rev. Sci. Instrum.* **1995**, *66*, 3584; b) K. Luo, Z. Shi, J. Lai, A. Majumdar, *Appl. Phys. Lett.* **1996**, *68*, 325; c) Y. Suzuki, *Japanese*

© 2019 The Authors. Published by WILEY-VCH Verlag GmbH & Co. KGaA, Weinheim

J. Appl. Phys. **1996**, *35*, L352; d) M. Lederman, D. Richardson, H. C. Tong, *Magn. IEEE Trans.* **1997**, *33*, 2923; e) K. Luo, Z. Shi, J. Varesi, A. Majumdar, *J. Vac. Sci. Technol., B: Microelectron. Nanometer Struct.* **1997**, *15*, 349; f) M. Calvert, J. Baker, *J. Thermophys. Heat Transfer* **1998**, *12*, 138; g) G. Mills, H. Zhou, A. Midha, L. Donaldson, J. M. R. Weaver, *Appl. Phys. Lett.* **1998**, *72*, 2900; h) L. Shi, O. Kwon, A. Miner, A. Majumdar, *Microelectromech. Syst.* **2001**, *10*, 370.

[34] a) G. Mills, J. M. R. Weaver, G. Harris, W. Chen, J. Carrejo, L. Johnson, B. Rogers, *Ultramicroscopy* **1999**, *80*, 7; b) K. Edinger, T. Gotszalk, I. Rangelow, *J. Vac. Sci. Technol., B: Microelectron. Nanometer Struct.* **2001**, *19*, 2856; c) I. Rangelow, T. Gotszalk, P. Grabiec, K. Edinger, N. Abedinov, *Microelectron. Eng.* **2001**, *57–58*, 737; d) O. Nakabeppu, T. Suzuki, *J. Therm. Anal. Calorim.* **2002**, *69*, 727; e) A. Gaitas, Y. B. Gianchandani, *Ultramicroscopy* **2006**, *106*, 874.

[35] a) L. Aigouy, G. Tessier, M. Mortier, B. Charlot, *Appl. Phys. Lett.* **2005**, *87*, 184105; b) B. Samson, L. Aigouy, P. Löw, C. Bergaud, B. J. Kim, M. Mortier, *Appl. Phys. Lett.* **2008**, *92*, 023101; c) L. Aigouy, E. Saidi, L. Lalouat, J. Labeguerie-Egea, M. Mortier, P. Low, C. Bergaud, *J. Appl. Phys.* **2009**, *106*, 074301.

[36] O. Nakabeppu, M. Chandrachood, Y. Wu, J. Lai, A. Majumdar, *Appl. Phys. Lett.* **1995**, *66*, 694.

[37] K. Kim, W. Jeong, W. Lee, P. Reddy, *ACS Nano* **2012**, *6*, 4248.

[38] a) A. Assy, S. Gomès, *Nanotechnology* **2015**, *26*, 355401; b) R. Heiderhoff, H. Li, T. Riedl, *Microelectron. Reliab.* **2013**, *53*, 1413; c) J. Hirotani, J. Amano, T. Ikuta, T. Nishiyama, K. Takahashi, *Sens. Actuators, A* **2013**, *199*, 1; d) K. J. Kim, W. P. King, *Appl. Therm. Eng.* **2009**, *29*, 1631; e) F. Menges, H. Riel, A. Stemmer, C. Dimitrakopoulos, B. Gotsmann, *Phys. Rev. Lett.* **2013**, *111*, 205901; f) E. Puyoo, S. Grauby, J.-M. Rampnoux, R. Emmanuelle, S. Dilhaire, *Rev. Sci. Instrum.* **2010**, *81*, 073701; g) A. Wilson, Rensselaer Polytechnic Institute, Troy, New York **2017** ; h) A. I. Buzin, P. Kamasa, M. Pyda, B. Wunderlich, *Thermochim. Acta* **2002**, *381*, 9; i) M. Hofer, T. Ivanov, M. Rudek, D. Kopiec, E. Guliyev, T. P. Gotszalk, I. W. Rangelow, *Microelectron. Eng.* **2015**, *145*, 32; j) B. Nelson, W. P. King, *Rev. Sci. Instrum.* **2007**, *78*, 023702; k) Z. Dai, E. A. Corbin, W. P. King, *Nanotechnology* **2009**, *21*, 055503; l) G. Wielgoszewski, P. Sulecki, T. Gotszalk, P. Janus, D. Szmigiel, P. Grabiec, E. Zschech, *J. Vac. Sci. Technol., B* **2010**, *28*, C6N7; m) A. Gaitas, S. Gianchandani, W. Zhu, *Rev. Sci. Instrum.* **2011**, *82*, 053701; n) M. Timofeeva, A. Bolshakov, P. D. Tovee, D. A. Zeze, V. G. Dubrovskii, O. V. Kolosov, *Ultramicroscopy* **2016**, *162*, 42; o) Y.-S. Choi, X. Wu, D.-W. Lee, *Rev. Sci. Instrum.* **2014**, *85*, 045002; p) N. Barbosa, A. Slifka, *Microsc. Res. Tech.* **2008**, *71*, 579; q) P. Janus, A. Sierakowski, M. Rudek, P. Kunicki, A. Dzierka, P. Biczysko, T. Gotszalk, *Ultramicroscopy* **2018**, *193*, 104; r) P. Tovee, O. Kolosov, *Nanotechnology* **2013**, *24*, 465706; s) L. Vera-Londono, O. Caballero-Calero, J. Andrés Pérez-Taborda, M. Martín-González, *Coat. Thin-Film Technol.* **2019**, Ch. 1; t) P. Tovee, M. E. Pumarol, M. C. Rosamond, R. Jones, M. Petty, D. Zeze, O. Kolosov, *Phys. Chem. Chem. Phys.: PCCP* **2013**, *16*, 1174; u) E. N. Esfahani, F. Ma, S. Wang, Y. Ou, J. Yang, J. Li, *Natl. Sci. Rev.* **2018**, *5*, 59; v) S. Hamian, J. Yun, I. Park, K. Park, *Appl. Phys. Lett.* **2016**, *109*, 253114.

[39] a) G. S. Shekhawat, S. Ramachandran, H. Jiryaei Sharahi, S. Sarkar, K. Hujsak, Y. Li, K. Hagglund, S. Kim, G. Aden, A. Chand, V. P. Dravid, *ACS Nano* **2018**, *12*, 1760; b) T. P. Nguyen, L. Thiery, D. Teyssieux, D. Briand, P. Vairac, *J. Phys.: Conf. Ser.* **2017**, *785*, 012005; c) L. Thiery, N. Marini, J.-P. Prenel, M. Spajer, C. Bainier, D. Courjon, *Int. J. Therm. Sci.* **2000**, *39*, 519; d) H. Hwan Roh, J. Sik Lee, D. Lib Kim, J. Park, K. Kim, O. Kwon, S. Park, Y. Ki Choi, A. Majumdar, *J. Vac. Sci. Technol., B: Microelectron. Nanometer Struct.* **2006**, *24*, 2405; e) H. J. Kim, N. Moldovan, J. Felts, S. Somnath, Z. Dai, T. Jacobs, R. Carpick, J. Carlisle, W. P. King, *Nanotechnology* **2012**, *23*, 495302; f) K. Kim, J. Chung, J. Won, O. Kwon, J. Sik Lee, S. Park, Y. K. Choi, *Appl. Phys. Lett.* **2008**, *93*, 203115; g) K. Yoon, G. Hwang, J. Chung, H. G. Kim, O. Kwon, K. Kihm, J. Sik Lee, *Carbon* **2014**, *76*, 77.

[40] K. Sangjin, T. Ono, M. Esashi, *Rev. Sci. Instrum.* **2009**, *80*, 033703.

[41] a) N. Trannoy, A. Sayoud, M. Diaf, T. Duvaut, J. P. Jouart, P. Grossel, *Opt. Mater.* **2015**, *42*, 526; b) L. Aigouy, J. Lesueur, N. Bergeal, M. Mortier, *Appl. Phys. Lett.* **2012**, *101*, 123113; c) H. J. Lin, A. Assy, E. P. Lemaire, D. Briand, L. Billot, P. Gredin, M. Mortier, L. Aigouy, *2017 23rd Int. Workshop Therm. Invest. ICs Syst. (THERMINIC)*, IEEE, Amsterdam, Netherlands **2017**; d) E. Saïdi, B. Samson, L. Aigouy, S. Volz, P. Löw, C. Bergaud, M. Mortier, *Nanotechnology* **2009**, *20*, 115703.

[42] P. Tovee, C. Tinker-Mill, K. Kjoller, D. Allsop, P. Weightman, M. Surman, M. Siggel-King, A. Wolski, O. Kolosov, *Conden. Matter - Mesosc. Nanosc. Phys.* **2015**, *2*, 1.

[43] L. Han, Rensselaer Polytechnic Institute, Troy, New York, **2014**.

[44] a) P. Janus, D. Szmigiel, M. Weisheit, G. Wielgoszewski, Y. Ritz, P. Grabiec, M. Hecker, T. Gotszalk, P. Sulecki, E. Zschech, *Microelectron. Eng.* **2010**, *87*, 1370; b) J. Lee, W. P. King, *J. Microelectromech. Syst.* **2008**, *17*, 432; c) G. Bernhard Martin Fiege, A. Altes, R. Heiderhoff, L. Josef Balk, *J. Phys. D: Appl. Phys.* **1999**, *32*, L13; d) P. Vettiger, G. Cross, M. Despont, U. Drechsler, U. Durig, B. Gotsmann, W. Häberle, M. Lantz, H. Rothuizen, R. Stutz, G. Binnig, *IEEE Trans. Nanotechnol.* **2002**, *1*, 39.

[45] E. Brown, L. Hao, D. Cox, J. C. Gallop, *J. Phys.: Conf. Series* **2008**, *100*, 052012.

[46] A. Hammiche, D. Price, E. Dupas, G. Mills, A. Kulik, M. Reading, J. M. R. Weaver, H. Pollock, *J. Microsc.* **2000**, *199*, 180.

[47] a) W. P. King, B. Bhatia, J. Felts, H. J. Kim, B. Kwon, B. Lee, S. Somnath, M. Rosenberger, *Ann. Rev. Heat Transfer* **2013**, *12*, 287; b) S. Lefèvre, S. Volz, P.-O. Chapuis, *Int. J. Heat Mass Transfer* **2006**, *49*, 251.

[48] a) S. Gomès, N. Trannoy, P. Grossel, F. Depasse, C. Bainier, D. Charraut, *Int. J. Therm. Sci.* **2001**, *40*, 949; b) S. Lefevre, S. Volz, *Rev. Sci. Instrum.* **2005**, *76*, 033701; c) P.-O. Chapuis, S. Saha, S. Volz, in Therminic 2006, Proc. of 12th International Worshop on Thermal Investigations of ICs, September **2006**; d) Y. Zhang, C. Hapenciuc, E. Castillo, T. Borca-Tasciuc, R. Mehta, C. Karthik, G. Ramanath, *Appl. Phys. Lett.* **2010**, *96*, 062107; e) Y. Zhang, Rensselaer Polytechnic Institute, Troy, New York **2011**.

[49] G. Wielgoszewski, P. Sulecki, T. Gotszalk, P. Janus, P. Grabiec, M. Hecker, Y. Ritz, E. Zschech, *Phys. Status Solidi B* **2011**, *248*, 370.

[50] S. Gomès, P. O. Chapuis, F. Nepveu, N. Trannoy, S. Volz, B. Charlot, G. Tessier, S. Dilhaire, B. Cretin, P. Vairac, *IEEE Trans. Compon. Packag. Technol.* **2007**, *30*, 424.

[51] D. Cahill, *Rev. Sci. Instrum.* **2002**, *73*, 3701.

[52] a) M. Chirtoc, J. F. Henry, *Eur. Phys. J.: Spec. Top.* **2008**, *153*, 343; b) S. Lefevre, J. B. Saulnier, C. Fuentes, S. Volz, *Superlattices Microstruct.* **2004**, *35*, 283.

[53] a) Y. S. Ju, K. Kurabayashi, K. Goodson, *Thin Solid Films* **1999**, *339*, 160; b) S. Huxtable, A. R. Abramson, C.-L. Tien, A. Majumdar, C. LaBounty, X. Fan, G. Zeng, J. Bowers, A. Shakouri, E. T. Croke, *Appl. Phys. Lett.* **2002**, *80*, 1737.

[54] M. Nonnenmacher, K. Wickramasinghe, *Appl. Phys. Lett.* **1992**, *61*, 168.

[55] W. H. Wollaston, *Philos. Trans. R. Soc. London* **1813**, *103*, 114.

[56] a) P. Kamasa, A. Buzin, M. Pyda, B. Wunderlich, *Thermochim. Acta* **2002**, *381*, 139; b) A. Dazzi, R. Prazeres, F. Glotin, J. M. Ortega, *Opt. Lett.* **2005**, *30*, 2388.

[57] L. David, S. Gomès, M. Raynaud, *J. Phys. D: Appl. Phys.* **2007**, *40*, 4337.

[58] Y. Joliff, L. Belec, J. F. Chailan, *J. Surf. Eng. Mater. Adv. Technol.* **2011**, *1*, 1.

[59] J. Bodzenta, A. Kaźmierczak-Bałata, M. Lorenc, J. Juszczyk, *Int. J. Thermophys.* **2010**, *31*, 150.

© 2019 The Authors. Published by WILEY-VCH Verlag GmbH & Co. KGaA, Weinheim

[60] E. Puyoo, S. Grauby, J.-M. Rampnoux, R. Emmanuelle, S. Dilhaire, *J. Appl. Phys.* **2011**, *109*, 024302.
[61] Kelvin Nanotechnology Ltd. **2015**.
[62] A. Wilson, M. Rojo, B. Abad, J. Perez Taborda, J. Maiz, J. Schomacker, M. Martín-González, D.-A. Borca-Tasciuc, T. Borca-Tasciuc, *Nanoscale* **2015**, *7*, 15404.
[63] Y. Zhang, P. S. Dobson, J. M. R. Weaver, *J. Vac. Sci. Technol., B* **2011**, *30*, 010601.
[64] J. Chung, K. Kim, G. Hwang, O. Kwon, S. Jung, J. Lee, J. W. Lee, G. Tae Kim, *Rev. Sci. Instrum.* **2010**, *81*, 114901.
[65] M. Hinz, O. Marti, B. Gotsmann, M. A. Lantz, U. Dürig, *Appl. Phys. Lett.* **2008**, *92*, 043122.
[66] L. Ramiandrisoa, A. Allard, B. Hay, S. Gomés, *Meas. Sci. Technol.* **2017**, *28*, 115010.
[67] P. Borowicz, P. Janus, P. Grabiec, R. Dobrowolski, *Microelectron. Eng.* **2016**, *154*, 12.
[68] K. Hatakeyama, E. Sarajlic, M. H. Siekman, L. Jalabert, H. Fujita, N. Tas, L. Abelmann, *IEEE 27th Int. Conf. Micro Electro Mech. Syst. (MEMS)*, **2014**.
[69] M. Despont, J. Brugger, U. Drechsler, U. Dürig, W. Häberle, M. Lutwyche, H. Rothuizen, R. Stutz, R. Widmer, G. Binnig, H. Rohrer, P. Vettiger, *Sens. Actuators, A* **2000**, *80*, 100.
[70] A. Rodriguez, M. T. H. Reid, S. G. Johnson, *Phys. Rev. B* **2012**, 86.
[71] J. Juszczyk, M. Wojtol, J. Bodzenta, *Int. J. Thermophys.* **2013**, *34*, 620.
[72] H. J. Kim, Z. Dai, W. P. King, *J. Micromech. Microeng.* **2013**, *23*, 025001.
[73] S. Somnath, W. P. King, *Sens. Actuat. A Physical* **2012**, *192*, 23.
[74] a) E. T. Swartz, R. Pohl, *Rev. Mod. Phys.* **1989**, 61; b) A. Pavlov, *Appl. Phys. Lett.* **2004**, *85*, 2095.
[75] S. Sadat, A. Tan, Y. Jie Chua, P. Reddy, *Nano Lett.* **2010**, *10*, 2613.
[76] a) H. Zhou, A. Midha, G. Mills, S. Thoms, S. Murad, J. M. R. Weaver, *J. Vac. Sci. Technol., B: Microelectron. Nanometer Struct.* **1998**, *16*, 54; b) K. Ohmyoung, University of California at Berkeley, USA **2000**.
[77] A. Kittel, W. Mueller-Hirsch, J. Parisi, S.-A. Biehs, D. Reddig, M. Holthaus, *Phys. Rev. Lett.* **2005**, *95*, 224301.
[78] E. Oesterschulze, M. Stopka, L. Ackermann, W. Scholz, S. Werner, *J. Vac. Sci. Technol., B: Microelectron. Nanometer Struct.* **1996**, *14*, 832.
[79] L. Thiery, É. Gavignet, B. Cretin, *Rev. Sci. Instrum.* **2009**, *80*, 034901.
[80] A. Bontempi, T. P. Nguyen, R. Salut, L. Thiery, D. Teyssieux, P. Vairac, *Rev. Sci. Instrum.* **2016**, *87*, 063702.
[81] a) J. Gimzewski, C. Gerber, E. Meyer, R. R. Schlittler, *Chem. Phys. Lett.* **1994**, *217*, 589; b) R. Berger, C. Gerber, J. Gimzewski, E. Meyer, H. J. Güntherodt, *Appl. Phys. Lett.* **1996**, *69*, 40.
[82] E. Saïdi, J. Labéguerie-Egéa, L. Billot, J. Lesueur, M. Mortier, L. Aigouy, *Int. J. Thermophys.* **2012**, *34*, 259.
[83] D. Halbertal, J. Cuppens, M. Ben Shalom, L. Embon, N. Shadmi, Y. Anahory, H. R. Naren, J. Sarkar, A. Uri, Y. Ronen, Y. Myasoedov, L. Levitov, E. Joselevich, A. Konstantin Geim, E. Zeldov, *Nature* **2016**, *539*, 407.
[84] J. Wells, E. Selezneva, P. Krzysteczko, X. Hu, H. W. Schumacher, R. Mansell, R. Cowburn, A. Cuenat, O. Kazakova, *AIP Adv.* **2017**, *7*, 055904.
[85] J. Varesi, A. Majumdar, *Appl. Phys. Lett.* **1998**, *72*, 3739.
[86] B. Cretin, *Superlattices Microstuct* **2004**, *35*, 253.
[87] A. Dazzi, R. Prazeres, F. Glotin, J. M. Ortega, M. Sawaftah, M. Frutos, *Ultramicroscopy* **2008**, *108*, 635.
[88] A. Deniset-Besseau, C. Prater, M.-J. Virolle, A. Dazzi, *J. Phys. Chem. Lett.* **2014**, *5*, 654.
[89] S. H. Christie, *J. Phys. D: Appl. Phys.* **1833**, *123*, 95.
[90] W. Thomson, *Philos. Mag.* **1862**, *24*, 149.
[91] a) W. Mueller-Hirsch, A. Kraft, M. T. Hirsch, J. Parisi, A. Kittel, *J. Vac. Sci. Technol., A* **1999**, *17*, 1205; b) A. Kittel, U. Wischnath, J. Welker, O. Huth, F. Rüting, S. A. Biehs, *Appl. Phys. Lett.* **2008**, *93*, 193109.
[92] L. Worbes, D. Hellmann, A. Kittel, *Phys. Rev. Lett.* **2013**, *110*, 134302.
[93] J. Spiece, C. Evangeli, K. Lulla, A. Robson, B. Robinson, O. Kolosov, *J. Appl. Phys.* **2018**, *124*, 015101.
[94] S. Gomès, *Quantiheat Consortium, 23rd Int. Workshop Them. Invest. ICs Syst.,* September **2017**.
[95] J. Bodzenta, J. Juszczyk, A. Kaźmierczak-Bałata, G. Wielgoszewski, *Int. J. Thermophys.* **2014**, *35*, 2316.
[96] J. Martinek, M. Valtr, V. Hortvík, P. Grolich, D. Briand, M. Shaker, P. Klapetek, *Meas. Sci. Technol.* **2018**, *30*, 3.
[97] Y. Ge, University of Glasgow, England **2016**.
[98] P.-O. Chapuis, E. Rousseau, A. Assy, S. Gomès, S. Lefèvre, S. Volz, *MRS Online Proc. Libr. Arch.* **2013**, *1543*, 159.
[99] B. W. Chui, M. Asheghi, Y. S. Ju, K. E. Goodson, T. W. Kenny, H. J. Mamin, *Nanoscale Microscale Thermophys. Eng.* **1999**, *3*, 217.
[100] a) C.-Y. Zhu, Z.-Y. Li, W.-Q. Tao, *J. Heat Transf.* **2017**, *139*, 052405; b) W. D. Zhou, B. Liu, S. yu, W. Hua, *Phys. Rev. E: Stat., Nonlinear, Soft Matter Phys.* **2010**, *81*, 011204.
[101] a) V. Jean, S. Fumeron, K. Termentzidis, X. Zianni, D. Lacroix, *Int. J. Heat Mass Transfer* **2015**, *86*, 648; b) V. Jean, J. Randrianalisoa, N. Trannoy, *21st Int. Workshop Therm. Invest. ICs Syst.* (THERMINIC), Paris, September **2015**; c) L. Chen, G. Yang, J. Liu, X. Shu, G. Zhang, Y. Jiang, *J. Appl. Phys.* **2009**, *105*, 013513; d) N. Masters, W. Ye, W. P. King, *Phys. Fluids* **2005**, *17*, 100615.
[102] P.-O. Chapuis, J.-J. Greffet, K. Joulain, S. Volz, *Nanotechnology* **2006**, *17*, 2978.
[103] a) A. Assy, S. Lefevre, S. Gomès, *21st Int. Workshop Therm. Invest. ICs Syst.* (THERMINIC), Paris **2015**; b) A. Assy, S. Lefèvre, P.-O. Chapuis, S. Gomès, *21st Int. Workshop Therm. Invest. ICs Syst. (THERMINIC)*, Paris **2015**.
[104] L. Guo, X. M. Zhao, Y. Bai, L. Qiao, *Appl. Surf. Sci.* **2012**, *258*, 9087.
[105] a) M. Luna, J. Colchero, A. Baró, *J. Phys. Chem. B* **1999**, *103*, 9576; b) M. He, A. Blum, E. Aston, C. Buenviaje, R. M. Overney, R. Luginbuhl, *J. Chem. Phys.* **2001**, *114*, 1355.
[106] a) R. Prasher, *Nano Lett.* **2005**, *5*, 2155; b) B. Nelson, W. P. King, *Nanosc. Microsc. Therm.* **2008**, *12*, 98; c) S. K. Saha, L. Shi, *J. Appl. Phys.* **2007**, *101*, 074304; d) W. P. King, K. Goodson, *J. Heat Transf.* **2007**, *129*, 1600.
[107] P. Fletcher, B. Lee, W. P. King, *Nanotechnology* **2011**, *23*, 035401.
[108] K. Park, G. Cross, Z. M. Zhang, W. P. King, *J. Heat Transfer* **2008**, *130*, 102401.
[109] M. E. Pumarol, M. C. Rosamond, P. Tovee, M. Petty, D. Zeze, V. Falko, O. Kolosov, *Nano Lett.* **2012**, *12*, 2906.
[110] L. Shi, A. Majumdar, *Appl. Scanning Probe Methods* **2004**, 327.
[111] a) R. J. Stoner, H. J. Maris, *Phys. Rev. B: Condens. Matter* **1994**, *48*, 16373; b) M. Kelkar, P. Phelan, B. Gu, *Int. J. Heat Mass Transfer* **1997**, *40*, 2637; c) D. Cahill, W. K. Ford, K. Goodson, G. D. Mahan, A. Majumdar, H. J. Maris, R. Merlin, S. Phillpot, *J. Appl. Phys.* **2003**, *93*, 793.
[112] a) M. Mohammad Sadeghi, S. Park, Y. Huang, D. Akinwande, Z. Yao, J. Murthy, L. Shi, *J. Appl. Phys.* **2016**, *119*, 235101; b) H. Fischer, *Thermochim. Acta* **2005**, *425*, 69.
[113] a) J. R. Culham, M. Yovanovich, G. Schneider, *Appl. Mech. Rev.* **2006**, *59*, 1; b) A. M. Clausing, B. T. Chao, *J. Heat Transfer* **1965**, *87*, 243.
[114] B. N. J. Persson, A. I. Volokitin, H. Ueba, *J. Phys.: Condens. Matter* **2011**, *23*, 045009.
[115] J. Maassen, M. s. Lundstrom, *J. Appl. Phys.* **2014**, *117*, 035104.
[116] a) J. P. McKelvey, R. L. Longini, T. P. Brody, *Phys. Rev.* **1961**, *123*, 51; b) W. Shockley, *Phys. Rev. X* **1962**, *125*, 1570.
[117] K. C. Schwab, E. A. Henriksen, J. M. Worlock, M. Roukes, *Nature* **2000**, *404*, 974.
[118] a) G. Chen, *Nanoscale Energy Transport and Conversion A Parallel Treatment of Electrons, Molecules, Phonons, and Photons*, Massachusetts Institute of Technology, Oxford University Press, **2005**; b) C. Dames, G. Chen, *J. Appl. Phys.* **2004**, *95*, 682.
[119] I. Kai Hsu, M. T. Pettes, M. Aykol, C.-C. Chang, W.-H. Hung, J. Theiss, L. Shi, S. B. Cronin, *J. Appl. Phys.* **2011**, *110*, 044328.
[120] N. Brent, Georgia Institute of Technology, **2007**, *68*, 3353.

© 2019 The Authors. Published by WILEY-VCH Verlag GmbH & Co. KGaA, Weinheim

[121] A. Assy, S. Gomès, *Appl. Phys. Lett.* **2015**, *107*, 043105.
[122] S. Lefèvre, *Modélisation et élaboration des métrologies de microscopie thermique à sonde locale résistive,* Université de Poitiers, **2004**.
[123] J. C. Cuevas, F. J. García-Vidal, *ACS Photonics* **2018**.
[124] S. Shen, A. Narayanaswamy, G. Chen, *Nano Lett.* **2009**, *9*, 2909.
[125] L. Cui, W. Jeong, S. Hur, M. Matt, J. C. Klöckner, F. Pauly, P. Nielaba, J. Cuevas, E. Meyhofer, P. Reddy, *Science* (New York) **2017**, *355*, 1192.
[126] a) J.-P. Mulet, K. Joulain, R. Carminati, J.-J. Greffet, *Microscale Thermophys. Eng.* **2002**, *6*, 209; b) D. Polder, M. Van Hove, *Phys. Rev. B* **1971**, *4*, 3303; c) P. J van Zwol, G. Palasantzas, J. T. M. De Hosson, *Phys. Rev. E* **2008**, *78*, 031606.
[127] a) K. Kim, L. Cui, V. Fernández-Hurtado, *Nature* **2015**, *528,* 387; b) K. Kloppstech, N. Könne, S.-A. Biehs, A. W. Rodriguez, L. Worbes, D. Hellmann, A. Kittel, *Nat. Commun.* **2015**, *8*, 556; c) B. Song, A. Fiorino, E. Meyhofer, P. Reddy, *AIP Adv.* **2015**, *5*, 053503.
[128] K. Kloppstech, N. Könne, S.-A. Biehs, A. W. Rodriguez, L. Worbes, D. Hellmann, A. Kittel, *Nat. Comm.* **2017**, *8*, 14475.
[129] L. Cui, W. Jeong, V. Fernández-Hurtado, J. Feist, F. Garcia-Vidal, J. Cuevas, E. Meyhofer, P. Reddy, *Nat. Commun.* **2017**, *8*, 14479.
[130] a) P. Ho, T. Kwok, *Rep. Prog. Phys.* **1999**, *52*, 301; b) D. Gardner, J. D. Meindl, K. C. Saraswat, *IEEE Trans. Electron Devices* **1986**, *87*, 22091.
[131] A. Datas, D. Hirashima, K. Hanamura, *J. Therm. Sci. Technol.* **2013**, *8*, 91.
[132] S. Edalatpour, M. Francoeur, *J. Quant. Spectrosc. Radiat. Transfer* **2013**, 133.
[133] a) Github, http:\\github.com/HomerReid/buff-em; b) A. Polimeridis, M. T. H. Reid, W. Jin, S. G. Johnson, J. White, A. Rodriguez, *Phys. Rev. B* **2015**, *92*, 134202.
[134] a) S. Callard, G. Tallarida, A. Borghesi, L. Zanotti, *J. Non-Crystal. Solids* **1999**, *245*, 203; b) F. Depasse, P. Grossel, N. Trannoy, *Superlattices Microstruct.* **2004**, *35*, 269; c) K. Kim, J. Chung, G. Hwang, O. Kwon, J. Sik Lee, *ACS Nano* **2011**, *5*, 8700.
[135] F. P. Incropera, *Fundamentals of Heat and Mass Transfer*, Wiley, Hoboken, NJ **2007**.
[136] Y. Ge, Y. Zhang, J. Booth, J. M. R. Weaver, P. s. Dobson, *Nanotechnology* **2016**, *27*, 325503.
[137] K. Kim, W. Jeong, W. Lee, S. Sadat, D. Thompson, E. Meyhofer, P. Reddy, *Appl. Phys. Lett.* **2014**, *105*, 203107.
[138] J. Chung, K. Kim, G. Hwang, O. Kwon, Y. K. Choi, J. S. Lee, *Int. J. Therm. Sci.* **2011**, *62*, 109.
[139] P. Janus, A. Sierakowski, P. Grabiec, M. Rudek, W. Majstrzyk, T. Gotszalk, *Microelectron. Eng.* **2017**, *174*, 70.
[140] a) C. Wikle, *Handbook of Uncertainty Quantification* **2017**, p. 193; b) F. Menges, H. Riel, A. Stemmer, B. Gotsmann, *Rev. Sci. Instrum.* **2016**, *87*, 074902; c) S. Shen, *Ann. Rev. Heat Transf.* **2013**, *16*, 327.
[141] P. s. Dobson, G. Mills, J. M. R. Weaver, *Rev. Sci. Instrum.* **2005**, *76*, 054901.
[142] J. Bodzenta, J. Juszczyk, A. Kaźmierczak-Bałata, P. Firek, A. Fleming, M. Chirtoc, *Int. J. Thermophys.* **2016**, *37*, 17.
[143] a) M. Massoud, Lyon Institute of Nanotechnology, Lyon **2016**; b) D. Trefon-Radziejewska, J. Juszczyk, A. Fleming, N. Horny, J.-S. Antoniow, M. Chirtoc, A. Kaźmierczak-Bałata, J. Bodzenta, *Synth. Met.* **2017**, *232*, 72.
[144] a) D. Price, M. Reading, A. Hammiche, H. Pollock, *Int. J. Pharm.* **2000**, *192*, 85; b) V. V. Tsukruk, V. V. Gorbunov, N. Fuchigami, *Thermochim. Acta* **2002**, *395*, 151; c) H. Fischer, *J. Therm. Anal. Calorim.* **2008**, *92*, 625.
[145] S. Deshmukh, M. M. Rojo, E. Yalon, S. Vaziri, E. Pop, *IEEE Device Res. Conf. (DRC)*, Santa Barbara, CA, November **2018**.
[146] E. Yalon, S. Deshmukh, M. Rojo, F. Lian, C. M. Neumann, F. Xiong, E. Pop, *Sci. Rep.* **2017**, *7*, 15360.
[147] a) P. E. Puyoo, *Ecole Doctorale des Sciences Physiques et de l'Ingénieur*, Leon, France **2010**; b) S. Grauby, E. Puyoo, J.-M. Rampnoux, R. Emmanuelle, S. Dilhaire, *J. Phys. Chem. B* **2013**, *117*, 9025.
[148] Y. Ezzahri, L. Patino-Lopez, O. Chapuis, S. Dilhaire, S. Grauby, W. Claeys, S. Volz, *Superlattices Microstruct.* **2005**, *38*, 69.
[149] A. Varpula, A. Timofeev, A. Shchepetov, K. Grigoras, J. Hassel, J. Ahopelto, M. Ylilammi, M. Prunnila, *Appl. Phys. Lett.* **2017**, *110*, 262101.
[150] Y. Ge, Y. Zhang, J. M. R. Weaver, H. Zhou, P. s. Dobson, *J. Vac. Sci. Technol., B* **2015**, *33*, 06FA03.
[151] S. Lefevre, S. Volz, S. Jean Bernard, C. Fuentes, N. Trannoy, *Rev. Sci. Instrum.* **2003**, *74*, 2418.
[152] a) P. Klapetek, I. Ohlídal, J. Buršík, *Surf. Interface Anal.* **2006**, *38*, 383; b) K. Goodson, M. I. Flik, L. T. Su, D. Antoniadis, *IEEE Electron Device Lett.* **1993**, *253*, 29.
[153] a) A. A. Wilson, T. Borca-Tasciuc, *Rev. Sci. Instrum.* **2017**, *88*, 074903; b) S. Heisig, H. U. Danzebrink, A. Leyk, W. Mertin, S. Münster, E. Oesterschulze, *Ultramicroscopy* **1998**, *71*, 99.
[154] M. Thompson Pettes, L. Shi, *J. Heat Transfer* **2013**, *136*, 032401.
[155] F. Yang, C. Dames, *Phys. Rev. B* **2015**, *91*, 14.
[156] B. Gotsmann, M. Lantz, A. Knoll, U. Dürig, *Nanotechnology* **2010**, 66.
[157] a) M. M. Rojo, J. Martín, S. Grauby, T. Borca-Tasciuc, S. Dilhaire, M. Martin-Gonzalez, *Nanoscale* **2014**, *6*, 7858; b) K. Xu, S. Ye, L. Lei, L. Meng, S. Hussain, Z. Zheng, H. Zeng, W. Ji, R. Xu, Z. Cheng, *Nanoscale* **2018**, *10*, 13548; c) Y. Liu, M. Zhang, A. Ji, F. Yang, X. Wang, *RSC Adv.* **2016**, *6*, 48933.
[158] a) E. Yalon, C. J. McClellan, K. K. H. Smithe, M. Rojo, R. Lily Xu, S. Suryavanshi, A. Gabourie, C. M. Neumann, F. Xiong, A. Barati Farimani, E. Pop, *Nano Lett.* **2017**, *17*, 113081; b) I. Jo, M. T. Pettes, J. Kim, K. Watanabe, T. Taniguchi, Z. Yao, L. Shi, *Nano Lett.* **2013**, *13*, 550; c) Y.-J. Yu, M. Y. Han, S. Berciaud, A. B. Georgescu, T. Heinz, L. E. Brus, K. Kim, P. Kim, *Appl. Phys. Lett.* **2011**, *99*, 183105.
[159] a) A. A. Balandin, S. Ghosh, W. Z. Bao, I. Calizo, D. Teweldebrhan, F. Miao, C. N. Lau, *Nano Lett.* **2008**, *8*, 902; b) W. Cai, A. Moore, Y. Zhu, X. Li, S. Chen, L. Shi, R. Ruoff, *Nano Lett.* **2010**, *10*, 1645.
[160] L. Shen, S. Di, Y. Longxiang, X. Liu, G. Du, *Silicon Nanoelectronics Workshop (SNW)*, Kyoto, Japan, January **2018**.
[161] M. Tortello, S. Colonna, M. Bernal, J. Gómez, M. Pavese, C. Novara, F. Giorgis, M. Maggio, G. Guerra, G. Saracco, R. S. Gonnelli, A. Fina, *Carbon* **2016**, *109*, 390.
[162] K. M. F. Shahil, A. Balandin, *Solid State Commun.* **2012**, *152*, 1331.
[163] a) S. Gomès, L. David, V. Lysenko, A. Descamps-Mandine, T. Nychyporuk, M. Raynaud, *J. Phys. D: Appl. Phys.* **2007**, *40*, 6677; b) S. Gomès, P. Newby, B. Canut, K. Termentzidis, O. Marty, L. Fréchette, P. Chantrenne, V. Aimez, J. M. Bluet, V. Lysenko, *Microelectron. J.* **2013**, *44*, 1029.
[164] A. M. Massoud, J. M. Bluet, V. Lacatena, M. Haras, J. F. Robillard, P. O. Chapuis, *Appl. Phys. Lett.* **2017**, *111*, 063106.
[165] D. Choi, N. Poudel, S. B. Cronin, L. Shi, *Appl. Phys. Lett.* **2017**, *110*, 073104.
[166] K. K. H. Smithe, S. Suryavanshi, M. Rojo, A. D. Tedjarati, E. Pop, *ACS Nano* **2017**, *11*, 8456.
[167] E. Pop, *Nano Res.* **2010**, *3*, 147.
[168] S. Vaziri, E. Yalon, M. M. Rojo, S. V. Suryavanshi, H. Zhang, C. J. McClellan, C. S. Bailey, K. K. H. Smithe, A. J. Gabourie, V. Chen, S. Deshmukh, L. Bendersky, A. V. Davydov, E. Pop, *Sci. Adv.* **2019**, *5*, 1325.
[169] P. Yasaei, A. A. Murthy, Y. Xu, R. dos Reis, G. S. Shekhawat, V. P. Dravid, *Adv. Mater.* **2019**, *31*, 1808244.
[170] D. S. Choi, N. Poudel, S. Park, D. Akinwande, S. B. Cronin, K. Watanabe, T. Taniguchi, Z. Yao, L. Shi, *ACS Appl. Mater. Inter.* **2018**, *10*, 11101.
[171] D. Varandani, K. Agarwal, J. Brugger, B. Raj Mehta, *Rev. Sci. Instrum.* **2016**, *87*, 084903.

© 2019 The Authors. Published by WILEY-VCH Verlag GmbH & Co. KGaA, Weinheim

[172] M. Rojo, S. Grauby, J. M. Rampnoux, O. Caballero-Calero, M. Martín-González, S. Dilhaire, *J. Appl. Phys.* **2013**, *113*, 054308.
[173] K. Park, G. Hwang, H. Kim, J. Kim, W. Kim, S. Kim, O. Kwon, *Appl. Phys. Lett.* **2016**, *108*, 071907.
[174] J. Perez Taborda, M. Rojo, J. Maiz, N. Neophytou, M. Martín-González, *Sci. Rep.* **2016**, *6*, 32778.
[175] S. Ghaderi, K. Hassan, X. Han, J. Wang, L. Šiller, S. H. Olsen, *AIP Adv.* **2018**, *8*, 065221.
[176] Y. Kim, W. Jeong, K. Kim, W. Lee, P. Reddy, *Nat. Nanotechnol.* **2014**, *9*, 881.
[177] N. Kempf, C. Karthik, B. Jaques, J. Gigax, L. Shao, D. Butt, R. He, D. Wang, Z. Ren, Y. Zhang, *Appl. Phys. Lett.* **2018**, *112*, 243902.
[178] a) C. Jensen, M. Chirtoc, N. Horny, J.-S. Antoniow, H. Pron, H. Ban, *J. Appl. Phys.* **2013**, *114*, 133509; b) C. Jensen, M. Chirtoc, J.-S. Antoniow, H. Ban, *Int. J. Thermophys.* **2012**, *34*, 597.
[179] J.-L. Battaglia, A. Saci, M. Longo, A. Kusiak, R. Fallica, *Appl. Phys. Lett.* **2014**, *104*, 263103.
[180] J.-L. Battaglia, A. Saci, I. De, R. Cecchini, S. Selmo, M. Fanciulli, S. Cecchi, M. Longo, *Phys. Status Solidi A* **2016**, *213*, 335.
[181] S.-H. Lee, Y. Jung, R. Agarwal, *Nat. Nanotechnol.* **2007**, *2*, 626.
[182] S. W. Fong, C. M. Neumann, E. Yalon, M. Rojo, E. Pop, H. S. P. Wong, *IEEE Trans. Electron Devices* **2017**, *64*, 4496.
[183] I. M. Datye, M. Rojo, E. Yalon, M. J. Mleczko, E. Pop, *76th Device Res. Conf. (DRC)*, Santa Barbara, CA, USA, June **2018**, p. 1.
[184] K. Nakanishi, A. Kogure, T. Fujii, R. Kokawa, K. Deuchi, R. Kuwana, H. Takamatsu, *J. Nanobiotechnol.* **2013**, *11*, 33.
[185] K. Nakanishi, A. Kogure, R. Kuwana, H. Takamatsu, K. Ito, *Biocontrol Sci.* **2017**, *22*, 175.
[186] W. Häberle, M. Pantea, J. Hoerber, *Ultramicroscopy* **2006**, *106*, 678.
[187] D. L. Xu, X. Fu, C. Y. Xu, S. Q. Wang, J. Sun, D. G. Zhou, *Chem. Ind. Forest Prod.* **2015**, *35*, 1.
[188] D. Xu, Y. Zhang, H. Zhou, Y. Meng, S. Wang, *Holzforschung* **2016**, *70*, 323.
[189] D. Xu, C. Xu, T. Ding, Y. Zhang, S. Wang, *Linye Kexue/Scientia Silvae Sinicae* **2018**, *54*, 105.
[190] M. Boutaous, S. Gomès, Z. Refaa, M. Zinet, P. Bourgin, *ASME Int. Mech. Eng. Congr. Expo., Proc. (IMECE)*, San Diego, California, USA, November **2013**.
[191] A. Dawson, M. Rides, A. Maxwell, A. Cuenat, A. R. Samano, *Polym. Test.* **2015**, *41*, 198.
[192] C. Hongo, M. Kotera, Y. Urushihara, D. Izumo, T. Nishino, *Proc. SPIE*, Houston, Texas, May **2014**.
[193] S. S. Kharintsev, E. A. Chernykh, A. Fishman, S. Saikin, A. M. Alekseev, M. Salakhov, *J. Phys. Chem. C* **2017**, *121*, 3007.
[194] Y. Li, N. Mehra, T. Ji, X. Yang, L. Mu, J. Gu, J. Zhu, *Nanoscale* **2017**, *10*, 1695.
[195] W. Jeong, K. Kim, Y. Kim, W. Lee, P. Reddy, *Sci. Rep.* **2014**, *4*, 4975.
[196] S. Crossley, T. Usui, B. Nair, S. Kar-Narayan, X. Moya, S. Hirose, A. Ando, N. D. Mathur, *Appl. Phys. Lett.* **2016**, *108*, 032902.
[197] M. Mizuguchi, S. Ohata, K.-i. Uchida, E. Saitoh, K. Takanashi, *Appl. Phys. Exp.* **2012**, *5*, 3002.
[198] Q. Weng, K.-T. Lin, K. Yoshida, H. Nema, S. Komiyama, S. Kim, K. Hirakawa, Y. Kajihara, *Nano Lett.* **2018**, *18*, 4220.

© 2019 The Authors. Published by WILEY-VCH Verlag GmbH & Co. KGaA, Weinheim